Revision 2

Bentonite evolution at elevated pressures and temperatures: An experimental study for generic nuclear repository designs

Michael C. Cheshire[1], Florie A. Caporuscio[1], Michael S. Rearick[1], Carlos Jove-Colon[2], and Mary Kate McCarney[3]

[1] Los Alamos National Laboratory, Earth and Environmental Sciences, MS J966, Los Alamos, NM, 87545

[2] Sandia National Laboratory, Nuclear Waste Disposal Research and Analysis Department, MS 0779, Albuquerque, NM, 87185

[3] University of Wyoming, Department of Geology and Geophysics, Laramie, WY, 82071

Abstract

Geologic disposal of spent nuclear fuel in high capacity metal canisters may reduce the repository footprint, but it may yield high thermal loads (up to 300°C). The focus of this experimental work is to expand our understanding of the hydrothermal stability of bentonite clay barriers interacting with metallic phases under different geochemical, mineralogical, and engineering conditions. The hydrothermal experiments were performed using flexible Au/Ti Dickson reaction cells mounted in an externally-heated pressure vessel at 150 – 160 bars and temperatures up to 300°C for five to six weeks. Unprocessed Wyoming bentonite, containing primarily montmorillonite with minor amount of clinoptilolite, was saturated with a K-Ca-Na-Cl-bearing water (~1,900 mg/L total dissolved solids) at a 9:1 water:rock mass ratio. The bentonite and solution combination contained either steel plates or Cu-foils and were buffered to low Eh using magnetite and metallic iron. During reactions, pH, K^+, and Ca^{2+} concentrations decreased, whereas $SiO_{2(aq)}$, Na^+, and SO_4^{2-} concentrations increased throughout the experiments. Pyrite decomposition was first observed at ~210°C, generating $H_2S_{(aq,g)}$ that interacted with metal plates or evolves as a gas. The aqueous concentrations of alkali and alkaline earth cations appear to be buffered via montmorillonite and clinoptilolite exchange reactions. Illite or illite/smectite mixed-layer formation was significantly retarded in the closed system due to a limited K^+ supply along with high Na^+ and $SiO_{2(aq)}$ concentrations. Precursor clinoptilolite underwent extensive recrystallization during the six week, 300°C experiments producing a Si-rich analcime in addition to authigenic silica phases (i.e., opal, cristobalite). Analcime and feldspar formation partially sequester aqueous Al^{3+}, thereby potentially inhibiting illitization. Associated with the zeolite alteration is a ~ 17 % volume decrease (quartz formation) that translates into ~ 2% volume loss in the bulk bentonite. These results provide chemical information that can be utilized in extending the bentonite barriers' lifetime and thermal stability. Zeolite alteration mineralogy and illitization retardation under these experimental conditions is important for the evaluation of clay barrier long-term stability in a spent nuclear fuel repository.

Keywords: Analcime, Bentonite, Clinoptilolite, Electron microscopy, Hydrothermal, Illite/smectite, Montmorillonite, Nuclear Repository, X-ray powder diffraction

Introduction

The United States' Department of Energy (DOE) has recently initiated the evaluation of various generic options for deep geological repositories for the permanent disposition of used nuclear fuel. The development and evaluation of engineered barrier system (EBS) design concepts and their potential interactions with the natural barrier or with other EBS interfaces are inherently important to the long-term (i.e., tens of thousands of years) safety and performance of geological repositories (Jové-Colón et al. 2011; Nutt et al. 2011).

The exact barrier concept has yet to be determined, but the U.S. has considered the possible use of dual purpose canisters for storage and subsequent disposal (Greenburg and Wen 2013). At present, dual purpose canister designs vary greatly, but, in most cases canisters will be constructed from steel or stainless steel with a steel reinforced concrete overpack (IAEA 2000). In some designs, copper cladding can be added on to the steel canister (Pusch 2008). These canisters can have up to 32 spent fuel assemblies (32 pressurized water reactors or 32-PWR), while many of the European concepts are limited to four spent fuel assemblies (4-PWR) (Pusch 2008; Greenburg and Wen 2013). This increased number of spent fuel assemblies will generate a greater amount of heat radiating into the host rock. High-level modeling suggests a 32-PWR waste package (at 60 gigawatt-days per metric ton burnup) disposed in a clay/shale host rock, has the potential to reach 299°C after 85 years within 1 meter from the waste package (25 years ventilation; 15 m package spacing; Greenberg and Wen 2013). These results are just one of many models or designs for a U.S. nuclear repository, but, this particular model provides one possible high temperature scenario.

One of the more commonly proposed ideas for permanent high-level nuclear waste disposal is to emplace the steel waste canister in a geological repository with a bentonite barrier between the canister and host rock (Pusch 1979; Meunier et al. 1998). Bentonite is used to provide a physical barrier to prevent fluid seeping in from natural surroundings and interacting with the waste package, while acting as a chemical barrier by attenuating actinide migration if a release occurs. Additionally, the bentonite's swelling capacity has the capability of self-sealing if cracks develop within the bentonite due to shrink-swell phenomena. However, there remain uncertainties regarding the long-term stability of bentonite under potential repository conditions, particularly, under prolonged periods of high thermal loads. There have been numerous investigations on the stability of bentonites under various repository conditions and in contact with various metals replicating possible canister compositions (Pusch 1979; Madsen 1998; Meunier et al. 1998; Guillaume et al. 2003; Wersin et al. 2007; Mosser-Ruck et al. 2010; Ferrage et al. 2011).

The focus of this experimental work is to expand our understanding on bentonite's stability under a variety of geochemical, mineralogical, and engineering conditions simulating possible nuclear repository environments. Alteration of smectite to other minerals (i.e., illite, illite/smectite, chlorite), silica cementation, steam-induced swelling loss, and interaction of smectite with metal waste canisters are some of the more prevalent concerns (Couture 1985; Wersin et al. 2007; Mosser-Ruck et al. 2010). This communication addresses the various authigenic minerals occurring within an unprocessed Wyoming bentonite during hydrothermal investigations replicating a high temperature repository-like environment.

Methods

Experimental setup

The bentonite used in this experimental work is mined from a reducing horizon in Colony, Wyoming. The bentonite was pulverized and sieved to < 3 mm and used with a free moisture of ~15.5 wt. %. The synthetic solution composition was chosen to represent that of a deep groundwater in crystalline rock (Table 1, Stripa sample V2 (69-4), Frape et al. 2003). The groundwater solution was prepared using reagent-grade salts dissolved in double deionised water. KOH and HCl were added to adjust the initial solution pH. This solution was then filtered through a 0.45 μm filter size and sparged with He to remove dissolved oxygen before each experiment. Two separate solutions were produced due to the experimental timing and quantities required (Table 1). The salt solution was added at a 9:1 water: bentonite mass ratio.

The redox conditions for each system were buffered using a 1:1 mixture (by mass) of Fe_3O_4 and iron-filings added at 7 wt. % of the bentonite mass. Approximately 7 wt. % (of total mass) 304 stainless steel (NIST SRM 101g), 316 stainless steel (NIST SRM 160b), Cu-foil, and low-carbon steel (provided by Sandia National Laboratory) were added to the experiments to mimic the presence of a waste canister.

Reactants (Table 2) were loaded into either a flexible gold or titanium reaction cell and fixed into a 500 mL Gasket Confined Closure reactor (Seyfried et al. 1987). Experiments were pressurized to 150 - 160 bar (mimicking lithostatic pressures for a shallow repository) and were heated following two different temperature profiles: 1) ramped: 120°C for two weeks, 210°C for two weeks, and then 300°C for one week and 2) isothermal: 300°C for six weeks (Figure 1). Reaction liquids were sampled (4 - 5 grams per sampling) during the experiments and analyzed to investigate the aqueous geochemical evolution in relationship to mineralogical alterations. The sampled reaction liquids were split three-ways producing aliquots for unfiltered anion, unfiltered

cation, and filtered (0.45 μm syringe filter) cation determination. All aliquots were stored in Teflon vials and kept at 1°C until analysis.

Mineral analyses

X-ray diffraction (XRD) analyses of experimental materials determined mineral compositions. Each sample was ground with 20 wt. % corundum for quantitative XRD analysis of the bulk rock (Chung 1974). XRD measurements were conducted with a Siemens D500 diffractometer using Cu-Kα radiation. Data were collected from 2 to 70 °2θ with a 0.02 °2θ step-size and count times of 8 to 12 seconds per step. To better analyze the non-clay and clay fractions, the < 2 μm particles were separated via sedimentation in DI H_2O. An aliquot of the < 2 μm suspension was dropped on a zero-background quartz plate and dried. This oriented mount was X-rayed from 2 to 40 °2θ at 8 to 12 s per step. The oriented mount was then saturated with ethylene glycol in a 60°C oven for 24 hours and XRD analysis was repeated. A portion of the > 2 μm particles was ground with a mortar/pestle, deposited on a zero-background quartz plate, and X-rayed under the same parameters as the bulk powder material. The remaining > 2 μm portion was used for electron microscopy. Mineral identification and unit-cell parameters analysis was performed using Jade© 7.5 X-ray data evaluation program with ICDD PDF-4 database. Quantitative phase analysis was performed using FULLPAT (Chipera and Bish 2002). The average mineral abundance error for each phase is approximately ±1 wt. % non-clay minerals and ±5 wt. % for clay minerals. Expandable component abundances were calculated via the Δ°2Θ method (Środoń 1980; Eberl et al. 1993; Moore and Reynolds 1997). Three separate regressions were used to calculate the % expandable (%Exp) component in each untreated and reacted bentonite. The equations are:

134 $\%Exp = 973.76 - 323.45\Delta + 38.43\Delta^2 - 1.62\Delta^3$ (Eberl et al. 1993, Eq. 3, R^2=0.99),

135 $\%Exp = 1517.8 - 548.49\Delta + 68.35\Delta^2 - 2.90\Delta^3$ (Eberl et al. 1993, Eq. 4, R^2=0.99), and

136 $\%Exp = 766.01 - 194.10\Delta + 12.924\Delta^2$ (Moore and Reynolds 1997, Table 8.3, R^2=.998),

137 with Δ corresponding to $\Delta°2\Theta$ between the 002 and 003 peak positions for the oriented, ethylene
138 glycol saturated samples.

139 X-ray florescence (XRF) analysis of the experimental materials was performed using a
140 Rigaku® ZSX Primus II. Samples were mixed with Li-metaborate at 7:1 or 36:1 and fluxed at
141 1,100°C for 45 minutes. All reported values exceed three times the reported detection limits. A
142 portion of the < 2 μm fraction from the reaction products and starting bentonite was analyzed to
143 determine the structural formulas following the methods described by Moore and Reynolds
144 (1997). All other starting materials were analyzed without separation. Loss on ignition (LOI) was
145 determined by heating the sample to 1,000°C for 30 minutes.

146 Electron microscopic analyses were performed using a FEI™ Inspect F scanning electron
147 microscope (SEM). All samples were Au-coated prior to SEM analysis. Imaging with the SEM
148 was performed using a 5.0 kV accelerating voltage and 1.5 spot size. Energy dispersive X-ray
149 spectroscopy (EDX) was performed at 30 kV and a 3.0 spot size.

150 Electron microprobe analyses were performed to determine the non-clay structural
151 compositions. Analyses were performed at University of Oklahoma using a Cameca® SX50
152 electron microprobe equipped with five wavelength-dispersive spectrometers and PGT PRISM
153 2000 energy-dispersive X-ray detector. Petrographic characterization was performed by
154 backscattered electron imaging coupled with energy-dispersive X-ray analysis, using beam
155 conditions of 20 kV acceleration and 20 nA sample current. Quantitative analysis was performed

by wavelength-dispersive spectrometry using 20 kV accelerating voltage, 20 nA beam current, and 2 μm spot size. Matrix corrections employed the PAP algorithm (Pouchou and Pichoir 1985), with oxygen content calculated by stoichiometry. Counting times were 30 seconds on peak for all elements, yielding minimum levels of detection (calculated at 3-σ above mean background) in the range of 0.01 to 0.03 wt% of the oxides for all components except F (0.16 wt%). All standards for elements in the silicates were analyzed using 30 second count times on peak, using Kα emissions. The standards and oxide detection limits are presented in the Appendix. Sodium analyses for clinoptilolite are problematic due to sodium migration under an electron beam, whereas analcime shows no sodium migration (Broxton et al. 1987). Zeolite structural formulae were calculated from data that have Al + Fe/(Na + K + 2*(Ca + Mg)) ratios within a range of 1.20 to 0.80.

Aqueous geochemical analyses

Major cations and trace metals were analyzed via inductively coupled plasma-optical emission spectrometry (Perkin Elmer® Optima 2100 DV) and inductively coupled plasma-mass spectrometry (Elan 6100) utilizing EPA methods 200.7 and 200.8. Ultra-high purity nitric acid was used in sample and calibration preparation prior to sample analysis. Internal standards (Sc, Ge, Bi, and In) were added to samples and standards to correct for matrix effects. Standard Reference Material (SRM) 1643e Trace Elements in Water was used to check the accuracy of the multi-element calibrations. Inorganic anion samples were analyzed by ion chromatography (IC) following EPA method 300 on a Dionex® DX-600 system. The reported raw aqueous chemical data were analyzed at room temperature and are not adjusted for *in situ* temperature effects. Unfiltered sample analyses were used for geochemical interpretations.

Equilibrium aqueous speciation and phase diagrams were performed via The Geochemist's Workbench® v.8.0.8 using a modified *thermo.dat* database. Reaction path modeling at 300°C (for Na^+, H^+ and $SiO_{2(aq)}$ activities) was performed via EQ3/6 (version 8.0; Wolery and Jarek 2003). Accurate thermodynamic modeling relies on databases that contain data compatible with the mineral hydration states, chemistries, and temperature ranges associated with the experimental system. However, existing standard state thermodynamic properties of complex clays and sheet silicates are still scarce and limited to low temperatures and specific compositions. In most cases, such data lacks the much-needed comprehensive characterization of the phase hydration state and mineral chemistry. Such limitation is exacerbated in the retrieval of high temperature thermodynamic data therefore imposing reliance on estimations based on oxide summations to generate data mainly for end-member compositions. Assessing the quality and adequacy of thermodynamic data for clays and zeolites is indeed a major subject of research that goes beyond the scope of this study. Still, internally-consistent thermodynamic data sets on clays and zeolites can provide the necessary information to construct activity phase diagrams having valid topologies to delineate equilibrium relations along with mapping of solution chemistries. Therefore, the standard GWB thermodynamic databases was adopted and also modified to incorporate minerals with compositions (e.g., analcime, illite) that are more consistent with those observed in these experiments (Neuhoff et al. 2004; Wilkin and Barnes 1998; Blanc and Vieillard 2010). However, end-member beidellite was used as the smectite phase in the phase diagrams instead of montmorillonite because of the importance for an internally consistent database and to simplify the system at higher temperatures.

Unfiltered solution chemistry data (analyzed at room temperature) were evaluated with the above-mentioned software and database to compute aqueous species activities at the

experimental temperatures. The computed species activities and activity ratios were plotted on phase diagrams to show the geochemical evolution of the fluid in the experiments. Pressures for the modeling are consistent with liquid-vapor saturation curve for water. Given the aforementioned limitations for data at high temperatures and pressures, the reaction path modeling of solution-mineral interactions should be treated as semi-quantitative even if it corroborates the experimental observations. These results highlight the need for experimental solubility and thermodynamic data for clays and zeolites at high temperatures and pressures.

Results

Mineralogy

The starting bentonite used in these experiments is a Na-montmorillonite with minor amounts of clinoptilolite, feldspars, biotite, cristobalite, quartz, and pyrite (Table 3). This material differs from the more commonly evaluated MX-80 bentonite by lacking calcite and gypsum, but contains significant amounts of clinoptilolite (Guillaume et al. 2004; Karnland 2010). There was no detected illite/smectite in the starting bentonite (Table 4). The montmorillonite displays the typical foily or 'cornflake' morphology associate with montmorillonite (Figure 2a). The bulk and < 2 μm bentonite compositions are listed in Table 5. Montmorillonite associated with this bentonite has a structural formula of $(Na_{0.31},Ca_{0.04},K_{0.01})(Al_{1.53},Fe_{0.21},Mg_{0.18},Ti_{0.01})(Si_{3.98},Al_{0.02})O_{10}(OH)_2$. Clinoptilolite in the bentonite appears to maintain the precursor volcanic shard morphology (Figure 2b) with a structural composition of $(Na_{4.30},Ca_{0.39},K_{0.14},Mg_{0.20})(Si_{29.82},Al_{6.28},Fe_{0.03})O_{72}\cdot nH_2O$ (n ~ 21, based on stoichiometric clinoptilolite). Feldspars are primarily albitic plagioclases $(Na_{0.71}Ca_{0.19}K_{0.07}(Si_{2.80}Al_{1.21})O_8)$ and K-feldspars $(K_{0.66}Na_{0.29}Ca_{0.01}(Si_{2.97}Al_{1.05})O_8)$. The bentonite

contains no more than 0.4 wt. % pyrite. There are two forms of pyrite in the starting bentonite: 1) framboidal pyrite (Figure 2c) and 2) cubic pyrite (Figure 2d).

Ramped Thermal Profile. There were no significant alterations to the montmorillonite away from the metal-bentonite interface. At the metal-bentonite interface there were significant changes to the phyllosilicates due to metal corrosion producing either Fe-phyllosilicates (i.e., Fe-saponite and chlorite) on steel surfaces or chalcocite on copper surfaces (unpublished data). The production and composition of these corrosion products are beyond the scope of this paper and will not be discussed in depth. The various reactions away from the bentonite-metal interface all showed similar mineralogical reactions indicating that the presence of metallic phases does not significantly influence the bulk bentonite (Table 3). The ethylene glycol saturated samples yielded d_{001} of 17 Å with a regular sequence of the $d_{00\ell}$ reflections (Figure 3). Additionally, the $\Delta^{o}2\Theta$ (002/003) values for post-reaction < 2 μm, ethylene glycol saturated fractions range from 5.21 to 5.29 $^{o}2\Theta$ corresponding to 98 to 106% expandable components (Table 4). The XRD data suggests that neither illite nor illite-smectite was produced during the reactions. Additionally, there appears to be no major morphological changes to the montmorillonite (Figure 4a). The structural formulae (calculated from XRF analyses of < 2 μm size separates (Table 5)) of the post-reaction montmorillonites has been summarized in Table 6. All structural iron has been assumed to be in the ferric-state. However, the true nature of this specific montmorillonite's structural iron is unknown and most likely contains both ferric to ferrous iron. Clinoptilolite maintains a similar composition to the starting clinoptilolite, but has a slight K^{+} and Ca^{2+} enrichment, $(Na_{3.05},K_{0.85},Ca_{0.74},Mg_{0.08})(Si_{29.92},Al_{6.23},Fe_{0.04})O_{72}\cdot nH_2O$.

Odor emanating from the aqueous samples and loss of pyrite in post-experiment samples suggests pyrite decomposition or dissolution occurred during each experiment yielding $H_2S_{(aq,g)}$.

248 Experiments containing stainless steel evolved $H_2S_{(g)}$ more readily due to limited interactions
249 with steel surfaces. Experiments with copper plates did not produce substantial $H_2S_{(g)}$ due to the
250 formation of chalcocite (Cu_2S) on the copper surfaces.

251 SEM evidence suggests that minor authigenic plagioclase is formed during these
252 reactions (Figure 4c). EMP analyses suggest plagioclases are albitic with a structural
253 composition of $(Na_{0.68}Ca_{0.26}K_{0.05})(Al_{1.25}Si_{2.75}Fe_{0.01})O_8$, while K-feldspars have an average
254 structural composition of $(K_{0.68}Na_{0.29}Ca_{0.01})(Al_{1.01}Si_{3.00})O_8$.

255 **Isothermal, 300ºC Profile**. Partial dissolution of the montmorillonite developed rough
256 edges during the long-term, isothermal 300°C experiments (Figure 6a). Structural formulas
257 presented in Table 6 have been adjusted for SiO_2 contribution from 5 wt. % opal-C/cristobalite
258 (indicated by XRD).

259 Ethylene glycol saturated samples yielded d_{001} of 17 Å with higher order $d_{00\ell}$ consistent
260 with integer values of the d_{001} values (Figure 5). Additionally, the $\Delta^o 2\Theta$ (002/003) values for
261 post-reaction < 2 μm, ethylene glycol saturated fractions range from 5.24 to 5.27 $^o2\Theta$
262 corresponding to 99 to 104% expandable components (Table 4). The XRD data of the ramped
263 and isothermal samples are indistinguishable and suggests that illite-smectite was not produced
264 during the reactions. However, there does appear to be a minor 10 Å peak present in the < 2 μm
265 fraction associated with EBS-5 (Figure 5, inset). SEM examination of the bulk material and > 2
266 μm fraction indicates minor amounts of an authigenic fibrous mineral. These fibers occur as
267 bundles or isolated fibers (Figure 6b). Fiber lengths span from 1.5 μm to 17.4 μm with widths
268 ranging from 0.10 μm to 0.51 μm, producing aspect ratios (l/w) from 15.5 to 55.5. Chemical
269 analyses of the discrete fibers were not collected due to the fiber thicknesses and the chemical
270 contribution from the underlying montmorillonite. The SEM and XRD data indicates authigenic

fibrous illite formed during the long-term, 300°C experiments. Considering the absence of illite-smectite mixed-layers in all experiments, the illite appears to be produced by direct crystallization.

Minor amounts of authigenic plagioclase appear to have formed during these reactions. EMP analyses suggest possible plagioclase overgrowths (Figure 6c) have an average structural formula of $(Na_{0.84},Ca_{0.16},K_{0.05})Al_{1.16}Si_{2.84}O_8$, while K-feldspars have an average structural composition of $(K_{0.67}Na_{0.27}Ca_{0.01})(Al_{1.02}Si_{3.00})O_8$.

Isothermal, 300°C experiments yielded analcime and opal-C/cristobalite as a result of an apparent dissolution of clinoptilolite and silica saturation (Cheshire et al. 2013):

$$\underset{\text{clinoptilolite}}{(Na_{4.30},Ca_{0.39},K_{0.14},Mg_{0.20})(Si_{29.82},Al_{6.28},Fe_{0.03})O_{72}\cdot 21H_2O} + 0.92\ Na^+ + 0.02\ Ca^{2+} \rightarrow$$

$$8.16\ \underset{\text{analcime}}{(Na_{0.64},Ca_{0.05})(Si_{2.23},Al_{0.77})O_6\cdot 1H_2O} + 0.14\ K^+ + 0.20\ Mg^{2+} + 11.62\ SiO_{2(aq)} + 12.64\ H_2O + 0.03\ Fe^{2+} + 0.40\ H^+$$

Analcime formed with an average Si/Al ratio of 2.93 (n = 18; σ = 0.08) with a calculated structural composition of $(Na_{0.64},Ca_{0.05})(Si_{2.23},Al_{0.76})O_6\cdot nH_2O$. Analcime occurs as 5 to 10 μm anhedral to subhedral trapezohedrons (Figure 6d). Anhedral analcime appears to form initially as an agglomeration of nano-sized, spherical crystals followed by coarsening of analcime nuclei to subhedral, trapezohedral analcime. Analcime can be seen both growing as isolated crystals in the montmorillonite groundmass and replacing the precursor clinoptilolite (Figure 6e).

Loss of pyrite in post-experiment samples and detection of odor in the aqueous samples suggests pyrite decomposition occurred during the experiments yielding $H_2S_{(aq,g)}$. Experiments containing stainless steel evolved $H_2S_{(g)}$ more readily, while experiments with copper plates did

not evolve substantial $H_2S_{(g)}$ due to the formation of chalcocite (Cu_2S) on the Cu surfaces (unpublished data).

Aqueous geochemistry

Aqueous geochemistry data is tabulated and is presented in the Deposit Item associated with this article. Key aqueous data is summarized here. Changes to the solution chemistry are fairly consistent between the different EBS experiments. There is an exchange of Na^+ for K^+ in the solution controlled by the cation exchange of both Na-montmorillonite and clinoptilolite (Figure 7a and 8a). This cation exchange yielded ~ 451 mg/L Na^+ enrichment and ~ 542 mg/L K^+ depletion in solution producing a K^+ enriched montmorillonite. There is also a decline in the Ca^{2+} aqueous concentrations (~76 mg/L) during experiments mostly likely due to montmorillonite cation exchange. The starting solution pH drops from ~ 8.2 to ~ 6.2 as the reaction progresses (see Deposit Item).

Silica ($SiO_{2(aq)}$) activity stays saturated with respect to cristobalite as the temperature increases (Figures 7b and 8b). Silica concentrations increase in increments closely following the temperature profile of the ramped heating cycle, indicating that silicate mineral dissolution is closely tied to the reaction temperature (Figure 7b). Maximum $SiO_{2(aq)}$ concentrations during the ramped experiments were ~ 1,054 mg SiO_2/L. During the 300°C experiments, $SiO_{2(aq)}$ concentrations rapidly increase to ~ 1,138 mg SiO_2/L and remained fairly steady for the experiment duration (Figure 8b). Silica activity significantly decreases upon quenching indicating precipitation of silica phases as the reaction cools.

316 Sulfur evolution is complicated by the occurrence of multiple redox states and interaction
317 with metallic phases, but appears to be primarily in the sulfide form during reactions. Total
318 sulfur concentrations (represented as sulfate) during the ramped experiments increased from ~47
319 mg/L to ~125 mg/L until reactions temperatures reached 300°C, when sulfur values dropped to
320 ~46 mg/L (Figure 9a). During the 300°C experiments, sulfur concentrations steadily climbed to a
321 ~191 mg/L. Aluminum concentrations tend to increase in increments closely following the
322 temperature profile during the ramped heating cycle (Figure 9b). The changes in aluminum
323 concentration are similar to the observed changes in the silica concentration. During the 300°C
324 experiments, aluminum concentrations rapidly increase to ~1.5 to 3.5 mg/L. After the initial
325 increase the aluminum concentrations slowly decreased. The decrease is likely related to the
326 crystallization of analcime, feldspars, and possible fibrous illite.

327

328 **Discussion**

329 Geochemical modeling

330 Aqueous sample collection during the experiments allows examination of aqueous
331 composition evolution in relation to mineralogical alteration. Both, aNa^+/aH^+ and aK^+/aH^+
332 activity ratios at 120°C tend to be scattered, but converge to a single solution composition as the
333 reaction progresses to 300°C (Figures 10 and 11). The $SiO_{2(aq)}$ composition becomes saturated
334 with respect to cristobalite beginning at around 210°C and the solution maintains cristobalite
335 saturation throughout the reaction process. This partially explains cristobalite crystallization
336 during the isothermal, 300°C reaction opposed to other silica formation.

Early during the reaction, aNa^+/aH^+ and silica activities are conducive for clinoptilolite alteration and Si-rich analcime crystallization (Figure 10). However, analcime formation was not observed except in the long-term, 300°C experiments, suggesting that analcime crystallization appears to be kinetically hindered. Results from these experiments agree with experimental work from Wilkin and Barnes (1998; 2000) indicating analcime formation is significantly retarded at circum-neutral pH's and increased pressures. Reaction path modeling (via EQ3/6) predicted silica activity increasing towards the high-Si analcime saturation boundary (Figure 10). It should be noted that the EQ3/6 reaction path runs were conducted using a slightly different thermodynamic database with specified mineral suppressions to simplify the system and to be consistent with the major mineralogy observed in the experiments. It is customary to apply mineral suppressions in geochemical modeling to simplify and maintain consistency with the observed phases in the mineral system of interest. This constrain also precludes the presence of phases that otherwise may be considered as metastable and could introduce inaccuracies in the reaction path calculation. The resulting topologies due to these suppressions are consistent with the EQ3/6 reaction path runs, but, are slightly different from those generated with GWB. Therefore, the overlay of the reaction path in Figure 10 is qualitative but representative of the predicted saturation sequence with respect to analcime and quartz along with the evolution of the fluid chemistry. Upon saturation or precipitation of high-Si analcime, the reaction model shows $\log aNa^+/H^+$ decreases until reaching saturation with respect to quartz, whereas, experimental data shows closer correspondence with respect to cristobalite. Quartz appeared to be the more stable silica phase in the code runs because quartz has a lower solubility than cristobalite. Given their relatively close solubilities, saturation with a Si-rich phase marks the termination of the

359 reaction path. The above reaction path is consistent with experimental observations of co-
360 existing high-Si analcime and $SiO_{2(xtl)}$ phases.

361 The aK^+/aH^+ activity ratios and aqueous silica activities early in the reaction plot within
362 the K-clinoptilolite stability field, but shifts into the illite ($K_{0.85}Al_2(Si_{3.15}Al_{0.85})O_{10}(OH)_2$)
363 stability field (Figure 11). However, much like the analcime formation, it is evident that the
364 solution chemistry imposes controls on illitization kinetics. Limited potassium and aluminum
365 availability along with high sodium and silica activities probably prevented the formation of an
366 illite-smectite transition state within the given reaction time. Direct precipitation of fibrous illite
367 appears to have occurred and consistent with the equilibrium phase topology and level of
368 saturation as depicted in Figure 11.

369

370 Absence of Smectite Illitization

371 There was no evidence of illite-smectite mixed-layering from any of the experiments
372 conducted in this investigation. It is evident that early in the experiments, K^+ is exchanged in the
373 montmorillonite interlayer generating a Na-rich solution and a K-bearing montmorillonite. Based
374 on changes to the structural formula (Table 6), only 11 to 20 % of the exchangeable cations in
375 the initial montmorillonite were replaced with K^+.

376 Many reports (Perry and Hower 1970; Reynolds and Hower 1970; Hower et al. 1976;
377 Altaner 1989; Mosser-Ruck et al. 2001) indicate smectite illitization occurs during diagenesis
378 under elevated temperatures with a reactive K^+ source via the following reaction scheme
379 (assuming aluminum conservation)

380

381 $1.617\ Na_{0.33}(Al_{1.67}Mg_{0.33})Si_4O_{10}(OH)_2 + 0.90\ K^+ + 0.502\ H^+ \rightarrow$
382 Na-montmorillonite

383 $K_{0.90}(Al_{1.90}Mg_{0.10})(Si_{3.20}Al_{0.80})O_{10}(OH)_2 + 3.268\ SiO_2 + 0.534\ Na^+ + 0.434\ Mg^{2+} + 0.868\ H_2O.$
384 illite

385

386 This general reaction is believed to go through a sequence starting with a K-montmorillonite
387 phase followed by various stages of illite-smectite mixed-layering leading into a discrete illite
388 phase (Moore and Reynolds 1997). Meunier et al (1998) has further suggested that high-charged
389 smectite (layer charges of 0.45-0.66 per $O_{10}(OH)_2$) develops just prior to the formation illitic
390 layers. Smectite-to-illite transformation is not well understood and probably follows several
391 different reaction pathways, i.e. solid-state transformation and dissolution-precipitation (Güven
392 2001; Dong 2005; Zhang et al. 2007). These different reaction mechanisms may be due to
393 different geological or experimental conditions, including variables such as water/rock ratio,
394 fluid composition, redox state, occurrence of microbial organisms, and presence or absence of
395 organic matter (Small et al. 1992; Small 1993; Güven 2001; Dong 2005; Zhang et al. 2007).
396 Solid-state transformation may be operative in closed systems, where the water/rock ratio is low,
397 whereas, dissolution-precipitation may be the dominant mechanism in open systems, where the
398 water/rock ratio is high (Zhang et al. 2007). In the current experiments, it appears that two major
399 parameters are preventing smectite-to-illite alteration: alkali and silica solution compositions.
400 **Alkali Effect.** Current experimental results are consistent with other experimental data
401 showing that a limited supply of K^+ along with a relatively high Na^+ activity significantly
402 decreases dioctahedral smectite illitization rates (Eberl and Hower 1977; Eberl 1978, Eberl et al.
403 1978; Roberson and Lahann 1981; Mosser-Ruck et al. 1999). Their studies also show that, in
404 general, dioctahedral smectites with low hydration-energy interlayer-cations (e.g., K^+, Rb^+, Cs^+)

405 are more susceptible to smectite-to-illite alteration reaction compared to dioctahedral smectites
406 with higher hydration-energy interlayer-cations (e.g., Na^{+}, Ca^{2+}, Mg^{2+}). However, the presence
407 of a Na-rich system does not preclude smectite illitization. There have been numerous
408 occurrences of illite and illite/smectite occurring in natural or experimental systems that are Na-
409 dominated (Bannister 1943; Frey 1969; Eberl and Hower 1977; Eberl et al. 1978; Whitney and
410 Velde 1993; Mosser-Ruck et al. 1999; Środoń 1999). But, in all these cases, either the
411 temperatures exceeded 300°C or there was a significant potassium source from groundwater or
412 coexisting minerals. Temperatures beyond 300°C exceed the upper temperature limits expected
413 for a repository environment and the experimental temperature from this investigation
414 (Greenburg and Wen 2013). Additionally, Na-bentonites are currently the bentonite of choice for
415 a repository backfill, thereby, providing a K-depleted and Na-enrich system. Even though the
416 aqueous solutions in the current experiments were K-rich, the overall system (bentonite + water)
417 was Na^{+} dominant (~ 2,400 mg Na/L) and K^{+} poor (~ 1,000 mg K/L). Include Ca^{2+} (~750 mg/L,
418 bentonite + water) in the discussion, the overall $(Na^{+} + Ca^{2+})/K^{+}$ ratio is greater than 3.0. It is
419 evident that the dominance of Na^{+} and Ca^{2+} along with the low abundance of K^{+} does not
420 facilitate illite-smectite formation after 45 days at 300°C.

421 **Silica Effect.** The silica activity in these experiments appears to be controlled partially by
422 silicate mineral dissolution and precipitation, in addition to clinoptilolite alteration. Solutions
423 saturated with respect to cristobalite probably contributed to illitization retardation in these
424 current experiments. Systems silica concentrations higher than quartz saturation have been
425 shown to significantly retard illitization rates (Eberl et al. 1978; Lahann and Roberson 1980;
426 Abercrombie et al. 1994). Abercrombie et al. (1994) has shown that a K-smectite to be the stable
427 phase, potentially up to 200°C, provided silica activity is higher than ~10^{-2}. It was noted by

Abercrombie et al. (1994) that as silica levels decreased, due to quartz precipitation, illitization progressed within the system. Therefore, an environment with silica concentrations saturated with respect to cristobalite at temperatures less than 300°C, such as the current experiments, smectite-to-illite alteration should further be inhibited. However, it is important to consider differences between closed, experimental systems versus geological or repository environments that open to the surrounding environment. Many processes that are observed in a closed, experimental system might be mitigated in an open system where solutes can freely move in and out of the environment.

Clinoptilolite-to-analcime transformation

We have shown that at higher silica activities (i.e., cristobalite saturation) clinoptilolite is altered to a high-silica analcime (Si/Al ~2.89) under experimental conditions. This zeolite alteration reaction has not been observed within a bentonite under repository-type experiments. The specifics of the clinoptilolite to analcime alteration have been discussed in detail (Smyth 1982; Chipera and Bish 1997; Wilkin and Barnes 1998; 2000; Bish et al. 2003; Cheshire et al. 2013) but, it is important to evaluate this analcime formation in context with the entire bentonite system. Previous studies (Smyth 1982; Kerrisk 1983; Duffy 1984; Bish and Aronson 1993; Wilkin and Barnes 1998; 2000) have linked changes in Na, Al, and Si activities with the replacement of clinoptilolite by analcime. Increased Na^+ activity under elevated temperatures (T > 84°C) has been suggested to promote alteration of clinoptilolite to analcime (Smyth 1982). Alternatively, it has been argued (Kerrisk 1983; Duffy 1984; Bish and Aronson 1993) that when silica activity is saturated with respect to quartz, clinoptilolite is destabilized relative to analcime. They (Kerrisk 1983; Duffy 1984; Bish and Aronson 1993) also suggested that when the silica

saturation is controlled by cristobalite or opal, clinoptilolite becomes more stable and analcime will not crystallize. However, experimental work ($T < 300°C$) from Wilkin and Barnes (1998) indicate silica activity influences clinoptilolite alteration by affecting the reaction affinity rather than controlling the reaction equilibrium. Wilkin and Barnes (1998) also show that analcime can form in an environment saturated with respect to cristobalite provided there is a sufficient change in the Na and/or Al activities. Additionally, phillipsite and analcime has been shown to crystallize in a FEBEX bentonite bearing volcanic glass under highly alkaline ($pH > 11.6$) and sodium-rich conditions (de la Villa et al. 2001). Analcime did not occur until the late-stages and higher temperatures of their experiments (de la Villa et al. 2001).

Silica is released during clinoptilolite alteration, thereby contributing to authigenic silica mineral formation (e.g., cristobalite, opal-C, quartz). There is a ~ 17 % volume decrease associated with analcime crystallization (analcime, 96.08 cm^3mol^{-1}, 1 H_2O; and clinoptilolite, 1,264.1 cm^3mol^{-1}, 21 H_2O; and quartz, 22.688 $cm^3\,mol^{-1}$) (Anderson 1996; Chipera and Bish 1997; Cheshire et al. 2013). Given that there is a ~ 13 wt. % clinoptilolite in the bentonite, a clinoptilolite-to-analcime volume loss should translate into ~ 2% volume loss in the bulk bentonite. It is uncertain how much volume loss will be recovered in response to the montmorillonite swelling due to the water loss (225 kg H_2O (0.8 wt. %) with 23,800 kg total backfill at 15 wt.% free moisture) in the zeolite alteration reaction, but a gross estimate using parameter set by Villar et al. (2012) indicates that the bentonite can swell 1 - 2 vol. % of its original volume (d-spacing change from 14.8 to 15.1 Å). If the estimate is correct, this calculation indicates that much of the lost volume could be recovered. Additionally, analcime and feldspar formation sequesters aqueous Al^{3+}, thereby potentially limiting illitization.

Aluminum sequestration, in addition to controls on silica, alkali, and alkaline earth activities, is probably a crucial step for the long-term stability of bentonite-based engineered barriers.

Silica evolution

The effect on the repository due the changes in the system's silica phases and concentrations appears to be significant issues regarding the repository stability and physical properties. In fact, it has been argued by Pusch et al. (1998) that smectite illitization will not constitute a major issue for the repository performance, but, cementation via silica precipitation poses as a greater risk to the repository stability and isolation capability. Silica precipitation has the potential to weld the smectite lamellae together and reduce the smectite expandability (Pusch et al. 1998; Pusch 2001). The primary mechanism suggested (Pusch et al. 1998; Pusch 2001) for silica liberation was illitization of smectite following the generalized reaction,

$$\text{Na-montmorillonite} + K^{+} + Al^{3+} \rightarrow \text{illite} + SiO_{2(aq)} + Na^{+} + H_2O.$$

However, many other mineral alteration/dissolution processes have significant controls on the silica concentrations when illitization does not occur. In the current work, illite-smectite mixed-layers were not observed, but, silica obtained cristobalite saturation primarily from clinoptilolite dissolution/alteration and a partial montmorillonite dissolution from the following generalized reactions,

$$\text{clinoptilolite} + Na^{+} \rightarrow \text{analcime} + K^{+} + SiO_{2(aq)} + H_2O,$$

495 $$\text{Na-montmorillonite} + H^+ + H_2O \rightarrow SiO_{2(am)} + Na^+ + Al^{3+} + Mg^{2+} + Fe^{2+/3+}.$$

496

497 Montmorillonite typically undergoes incongruent dissolution due to the preferential
498 leaching of the octahedral cations (i.e., Al^{3+}, Mg^{2+}, $Fe^{2+/3+}$) typically with an amorphous silica
499 residue (Kaviratna and Pinnavaia 1994; Bickmore et al. 2001; Marty et al. 2011). SEM evidence
500 suggests that smectite underwent limited dissolution during these experiments, but did not
501 undergo significant structural alteration. The reaction solution is under saturated with respect to
502 amorphous silica, thereby, forcing the amorphous silica phase to undergo dissolution via,

503

504 $$SiO_{2(am)} \rightarrow SiO_{2(aq)}.$$

505

506 No silica cementation was observed in these experiments, but, there is evidence for silica and
507 silicate formation. This is a very important consideration for nuclear repositories, because silica
508 cementation can cause decreased bentonite plasticity and permeability (Pusch et al. 1998; Pusch
509 2001). It has even been suggested to be a significant concern regarding repository stability when
510 considering mineral alterations (Pusch et al. 1998).

511

512 Sulfide destabilization

513 Production of $H_2S_{(aq,g)}$ is most likely related to pyrite solubility in water or a chloride-
514 bearing solution (Crerar et al. 1978; Ohmoto et al. 1994) and developing an acidic solution
515 following

516 $$FeS_{2(s)} + n\ Cl^-_{(aq)} + H_2O_{(aq)} \rightarrow FeCl_n^{2-n}{}_{(aq)} + 1/4\ H^+ + 1/4\ SO_4^{2-}{}_{(aq)} + 7/4\ HS^-_{(aq)},$$

517 $$FeS_{2(s)} + H_2O_{(aq)} \rightarrow Fe^{2+}_{(aq)} + 1/4\ H^+ + 1/4\ SO_4^{2-}{}_{(aq)} + 7/4\ HS^-_{(aq)},$$

518 $$H_2S_{(aq)} = H^+ + HS^-, \text{ and}$$

519 $$H_2S_{(g)} = H^+ + HS^-.$$

520 The solution pH's drop from ~8.2 (starting solution pH) to ~6.2 during the reaction
521 showing the production of H^+ is mostly likely and partially related to sulfide dissociation and
522 pyrite dissolution. Additionally, there are no carbonate minerals in this particular bentonite to
523 buffer the solution's pH. The highly reducing nature of the experimental system easily preserves
524 the $H_2S_{(aq,g)}$ and $HS^-_{(aq)}$ species. However, iron was not detected in the solution, indicating a sink
525 for the iron or concentrations below analytical detection limits. Sulfide-induced corrosion of the
526 waste canisters is the primary concern in repository systems (Börjesson et al. 2010). The
527 Swedish Nuclear Fuel and Waste Management Company (SKB) have enacted fairly strict sulfur
528 specifications (sulfide content < 0.5 wt.%; total sulfur < 1 wt.%) for the bentonite buffer used in
529 their repository design (Börjesson et al. 2010).

530

531 Potential effects on geological repository

532 After initial used-fuel emplacement there will be a pulse of heat flowing into the
533 bentonite buffer producing an environment in which montmorillonite does not typically occur.
534 However, many believe that the initial heat pulse will start to decay after about 100 to 1,000
535 years (Wersin et al. 2007). There have been a large number of investigations on bentonite
536 stability under various repository conditions (Madsen 1998; Meunier et al. 1998; Pusch and
537 Kasbohm 2002; Guillaume et al. 2003; 2004; Wilson et al. 2006; Marty et al. 2010; Mosser-Ruck
538 et al. 2010; Ferrage et al. 2011). Yet, questions remain regarding bentonite's overall stability and

more importantly whether montmorillonite will remain relatively unaltered through the repository life-time. Results from this investigation, along with the many other illitization and bentonite buffer investigations, indicate that if there is a reactive potassium source, there is a high likelihood of illitization occurring within the thermal limits associated with the initial used-fuel emplacement. Additionally, these same investigations indicate that if the system was engineered to have excess Na^+, Ca^{2+}, or Mg^{2+} with controls limiting K^+ availability, the montmorillonite and bentonite will be more stable and possibly experience limited illitization during the initial used-fuel emplacement. These are all good indications considering most bentonites proposed for repository backfill are Na/Ca-rich systems typically with low inherent potassium concentrations. Additionally, illitization reactions should be severely inhibited because repositories are expected to remain semidry (~15 wt.% free moisture) during the initial 100 to 1,000 years and display very low hydraulic conductivities (~3 x 10^{-13} m/s), thereby restricting K^+ and Al^{3+} redistribution or influx (Pusch and Kasbohm 2002; Wersin et al. 2007). Collectively, limited K^+ availability and a Na-rich system along with low hydraulic conductivity and other silicate mineral reactions should contribute to the bentonite buffer long-term stability.

Most often repository investigations focus on the MX-80 bentonite from Wyoming. The slightly different bentonite used in this investigation contains ~12 wt. % clinoptilolite, while MX-80 has ~2 wt. % calcite and no clinoptilolite. It is expected mineralogical variation will play a key role in the bentonite stability. For example, the presence of clinoptilolite develops reactions that have not been documented in bentonite clay barrier systems, even though clinoptilolite alteration has been well documented in other systems (Smyth 1982; Kerrisk 1983; Duffy 1984; Bish and Aronson 1993; Chipera and Bish 1997; Wilkin and Barnes 1998; 2000; Cheshire et al. 2013). Natural paragenetic sequences indicate that clinoptilolite to analcime may progress at

562 temperatures as low as 90 – 100°C (Smyth 1982). However, analcime formation does not occur
563 until the long-term, 300°C conditions, indicating high temperature reaction kinetics may be
564 important to the long-term repository EBS evaluation. The bentonite used in this investigation
565 did not contain carbonate minerals. Carbonate dissolution contributes to buffering groundwater
566 pHs, if carbonate is absent in the bentonite the pH buffering capacity is greatly diminished.
567 Alternatively, the presence of carbonate anions has been shown to strongly complex with various
568 actinides, thereby, increasing actinide mobility (Clark et al. 1995). In many cases it is difficult to
569 determine if the presence or loss of certain minerals will benefit or diminish a repository's long-
570 term stability.

571 There have been a number of similar investigations on bentonite stability under various
572 repository conditions and in contact with various metals replicating possible canister
573 compositions (Guillaume et al. 2003; 2004; Wilson et al. 2006a; 2006b; Mosser-Ruck et al.
574 2010; Ferrage et al. 2011). These investigations tend to focus on the Fe-bearing phases (i.e., Fe-
575 saponite, vermiculite, chlorite, and 7Å phases (odinite, berthierine, cronstedtite)) forming during
576 their experiments. Newly formed Fe-rich phyllosilicates in the current investigation are primarily
577 associated with the interface at steel plates and magnetite particles (unpublished results). Away
578 from these Fe-rich zones there was little to no clay alteration. These observations agree well with
579 the model results from Marty et al. (2010), in which the Fe-rich phases are associated with the
580 bentonite/steel interface. Bentonite not in contact with the steel waste container does not show
581 the formation of these Fe-rich phyllosilicates. A natural analogue of this relationship has been
582 described by del Villar et al. (2005) in which Fe,Mg-rich smectites formed proximal to a biotite-
583 hornblende dacite at temperature approaching 90°C. These authors argue that near the dacite
584 body the Mg and Fe concentrations increased facilitating the alteration of parent smectite.

585 However, distal portions of the parent smectite appear to maintain the initial smectite
586 composition (del Villar et al., 2005). The occurrence of Fe-rich phyllosilicates most likely will
587 not form in the bentonite away from the waste container because there is a low abundance of iron
588 in the system.

589 ## Conclusions

590 These experimental results demonstrate that understanding the mineralogical composition
591 of bentonite barrier materials and the possible alteration pathways is essential in designing a
592 high-level radioactive waste repository. The combination of a Na-rich environment, limited K
593 supply, and precipitation of Al-bearing minerals (analcime and feldspars) appear to have
594 inhibited the formation of illite-smectite mixed-layers. This geochemical information can then be
595 utilized in engineering a bentonite barrier with an extended lifetime and thermal stability. Illite
596 retardation is an important consideration in repository research as many researchers have argued
597 that illite formation is detrimental to the long-term stability of a used fuel repository. Even
598 though mineral reactions do take place, there are added properties that potentially will
599 compensate for the alteration of clinoptilolite to analcime (e.g., swelling of montmorillonite due
600 to water absorption and a potential of sealing/healing cracks via silica precipitation). Further
601 work needs to be done to better understand the kinetics of analcime formation in a bentonite
602 barrier system and what impact these reactions have on the barrier's mechanical and physical
603 properties.

604

605 ## Acknowledgements

We would like to thank Emily Kluk for XRF analyses and Liz Miller for assistance in the lab. Scanning electron microscopy facilities were provided by Materials Science and Technology group at Los Alamos National Laboratory. Dr. George Mason at the University of Oklahoma was instrumental in the obtaining of EMP analyses. Bentonite Performance Minerals, L.L.C. graciously provided the bentonite. We thank Drs. Dennis Newell and David Bish for the discussions regarding the experimental system and results. We also thank the two anonymous reviewers, whose suggestions improved this manuscript. Funding was through the Department of Energy's Used Fuel Disposition campaign. Los Alamos National Laboratory has assigned free release number LA-UR-13-23814 to this document.

References

Abercrombie, H.J., Hutcheon, I.E., Bloch, J.D., and de Caritat, P. (1994) Silica activity and the smectite-illite reaction. Geology, 22, 539-542.

Altaner, S.P. (1989) Calculation of K diffusional rates in bentonite beds. Geochimica et Cosmochimica Alta, 53, 923-931.

Anderson, G.M. (1996) Thermodynamics of Natural Systems. John Wiley & Sons, Inc., Canada, pp. 382.

Bannister, R.A. (1943) Brammalite (sodium-illite) a new mineral from Llandebie, South Wales. Mineralogical Magazine, 26, 304-307.

Bickmore, B.R., Bosbach, D., Hochella Jr., M.F., Charlet, L., and Rufe, E. (2001) In situ atomic force microscopy study of hectorite and nontronite dissolution: Implications for phyllosilicates edge surface structures and dissolution mechanisms. American Mineralogist, 86, 411-423.

Bish, D.L. and Aronson, J.L. (1993) Paleogeothermal and paleohydrologic conditions in silicic tuff from Yucca Mountain, Nevada. Clays and Clay Minerals, 41, 148-161.

Bish, D.L., Vaniman, D.T., Chipera, S.J., and Carey, J.W. (2003) The distribution of zeolites and their effects on the performance of a nuclear waste repository at Yucca Mountain, Nevada, U.S.A. American Mineralogist, 88, 1889-1902.

Blanc, P. and Vieillard, P. (2010) Thermochimie: Estimation of the thermodynamic properties of dehydrated phyllosilicates. Bureau de Recherches Géologiques et Miniéres Technical Report, RP-57798-FR, pp. 64.

Börjesson, L., Gunnarsson, D., Johannesson, L-E., and Jonsson, E. (2010) Design, production and initial state of the buffer. Svensk Kärnbränslehantering Technical Report, TR-10-15, pp. 89.

Broxton, D.E., Bish, D.L., and Warren, R.G. (1987) Distribution and chemistry of diagenetic minerals at Yucca Mountain, Nye County, Nevada. Clays and Clay Minerals, 35, 89-110.

Cheshire, M.C., Caporuscio, F.A., Jové-Colón, C., and McCarney, M.K. (2013) Alteration of clinoptilolite into high-silica analcime within a bentonite barrier system under used nuclear fuel repository conditions. Proceeding from the 14th International High-Level Radioactive Waste Management Conference, 410-415.

Chipera, S.J. and Bish, D.L. (1997) Equilibrium modeling of clinoptilolite-analcime equilibria at Yucca Mountain, Nevada, USA. Clays and Clay Minerals, 42, 226-239.

Chipera, S.J. and Bish, D.L. (2002) FULLPAT: a full-pattern quantitative analysis program for X-ray powder diffraction using measured and calculated patterns. Journal of Applied Crystallography, 35, 744–749.

Chung, F.H. (1974) Quantitative interpretations of X-ray diffraction patterns of mixtures. I. Matrix flushing method for quantitative multicomponent analysis. Journal of Applied Crystallography, 7, 519-525.

Clark, D.L., Hobart, D., and Neu, M.P. (1995) Actinide carbonate complexes and their importance in actinide environmental chemistry. Chemical Reviews, 95, 25-48.

Couture, R.A. (1985) Steam rapidly reduces the swelling capacity of bentonite. Nature, 318, 50-52.

Crerar, D.A., Susak, N.J., Borcsik, M., and Schwartz, S. (1978) Solubility of the buffer assemblage pyrite + pyrrhotite + magnetite in NaCl solution from 200 to 350°C. Geochimica et Cosmochimica Acta, 42, 1427-1437.

de la Villa, R.V., Cuevas, J., Ramirez, S., Leguey, S. (2001) Zeolite formation during the alkaline reaction of bentonite. European Journal of Mineralogy, 13, 635-644.

del Villar, L.P., Delgado, A., Reyes, E., Pelayo, M., Fernández-Soler, J.M., Cózar, J.S., Tsige, M., and Quejido, A.J. (2005) Thermochemically induced transformations in Al-smectite: A Spanish natural analogue of the bentonite barrier behavior in a radwaste disposal. Applied Geochemistry, 20, 2252-2282.

Dong, H. (2005) Interstratified illite-smectite: A review of contributions of TEM data to crystal chemical relation and reaction mechanisms. Clay Science, 12, Supplement 1, 6-12.

Duffy, C.J. (1984) Hydrothermal geochemistry. Research and Development Related to the Nevada Nuclear Waste Storage Investigation July 1 – September 30, 1982. Eds., Wolfsberg, K. and Vaniman, D.T. Los Alamos National Lab Report, LA-10032-PR, pp. 76.

Eberl, D. (1978) Reaction series for dioctahedral smectites. Clays and Clay Minerals, 26, 327-340.

Eberl, D. and Hower, J. (1977) The hydrothermal transformation of sodium and potassium smectite into mixed-layer clay. Clays and Clay Minerals, 25, 215-227.

Eberl, D., Whitney, G., and Khourym, H. (1978) Hydrothermal reactivity of smectite. American Mineralogist, 63, 401-409.

Eberl, D.D., Velde, B., and McCormick, T. (1993) Synthesis of illite-smecite from smectite at Earth surface temperatures and high pH. Clay Minerals, 28, 49-60.

Ferrage, E., Vidal, O., Mosser-Ruck, R., Cathelineau, M., and Cuadros, J. (2011) A reinvestigation of smectite illitization in experimental hydrothermal conditions: Results from X-ray diffraction and transmission electron microscopy. American Mineralogist, 96, 207-223.

Frape, S.K., Blyth, A., Blomqvist, R., McNutt, R.H., and Gascoyne, M. (2003) Deep Fluids in the Continents: II. Crystalline Rocks, Treatise on Geochemistry, 5, J. I. Drever, ed., 541-580.

Frey, M. (1969) A mixed-layer paragonite/phengite of low-grade metamorphic origin. Contribution to Mineralogy and Petrology, 24, 63-65.

Greenburg, H.R. and Wen, J. (2013) Repository layout and host rock thermal gradient trade study for large waste packages in clay/shale: Using the DSEF thermal analytical model. LLNL-TR-639869-DRAFT, pp. 38.

Guillaume, D., Neaman, A., Cathelineau, M., Mosser-Ruck, R., Peiffert, C., Abdelmoula, M., Dubessy, J., Villieras, F., Baronnet, A., and Michau, N., (2003) Experimental synthesis of chlorite from smectite at 300 ^{o}C in the presence of metallic Fe. Clay Minerals, 38, 281-302.

Guillaume, D., Neaman, A., Cathelineau, M., Mosser-Ruck, R., Peiffert, C., Abdelmoula, M., Dubessy, J., Villieras, F., and Michau, N., (2004) Experimental study of the transformation of smectite at 80 to 300 ^{o}C in the presence of Fe oxides. Clay Minerals, 39, 17-34.

Güven, N. (2001) Mica structure and fibrous growth of illite. Clays and Clay Minerals, 49, 189-196.

Hower, J., Eslinger, E.V., Hower, M.E., and Perry, E.A. (1976) Mechanism of burial metamorphism of argillaceous sediments. Geological Society of America Bulletin, 87, 725-737.

International Atomic Energy Agency (IAEA) (2000) Multi-purpose container technologies for spent fuel management. IAEA Technical Document, IAEA-TECDOC-1192, pp. 56.

Jové-Colón, C.F., et al. (2011) Disposal systems evaluations and tool development – engineered barrier system (EBS) evaluation (Fuel cycle research and development). Sandia National Laboratory, FCRD-USED-2011-000132, 16-48.

Karnland, O. (2010) Chemical and mineralogical characterization of the bentonite buffer for the acceptance control procedure in a KBS-3 repository. Svensk Kärnbränslehantering Technical Report, TR-10-60, pp. 29.

Kaviratna, H. and Pinnavaia, T.J. (1994) Acid hydrolysis of octahedral Mg2+ sites in 2:1 layered silicates: An assessment of edge attack and gallery access mechanisms. Clays and Clay Minerals, 42, 717-723.

Kerrisk, J.F. (1983) Reaction-path calculations of groundwater chemistry and mineral formation at Rainier Mesa, Nevada. Los Alamos National Lab Report, LA-9912-MS, pp. 41.

Lahann, R.W. and Roberson, H.E. (1980) Dissolution of silica from montmorillonite: effect of solution chemistry. Geochimica et Cosmochimica Acta, 44, 1937-1943.

Madsen, F.T. (1998) Clay mineralogical investigations related to nuclear waste disposal. Clay Minerals, 33, 109-129.

Marty, N.C.M., Cama, J., Sato, T., Chino, D., Villiéras, F., Razafitianamaharavo, A., Brendlé, J., Giffaut, E., Soler, J.M., Gaucher, E.C., and Tournassat, C. (2011) Dissolution kinetics of synthetic Na-smectite. An integrated experimental approach. Geochimica et Cosmochimica Acta, 75, 5849-5864.

Marty, N.C.M., Fritz, B., Clément, A., and Michau, N. (2010) Modelling the long term alteration of the engineered bentonite barrier in an underground radioactive waste repository. Applied Clay Science, 47, 82-90.

Meunier, A., Velde, B., and Griffault, L. (1998) The Reactivity of Bentonites: a Review. An Application to Clay Barrier Stability for Nuclear Waste Storage. Clay Minerals, 33, 187-196

Moore, D. M. and Reynolds, R.C. (1997) X-ray Diffraction and the Identification and Analysis of Clay Minerals. Oxford University Press, New York, New York, pp. 377.

Mosser-Ruck, R., Cathelineau, M., Baronnet, A., and Trouiller, A. (1999) Hydrothermal reactivity of K-smectite at 300°C and 100 bar: dissolution-crystallization process and non-expandable dehydrated smectite formation. Clay Minerals, 34, 275-290.

Mosser-Ruck, R., Cathelineau, M., Guillaume, D., Charpentier, D., Rousset, D., Barres, O., and Michau, N. (2010) Effects of Temperature, pH, and Iron/Clay and Liquid/Clay Ratios on Experimental Conversion of Dioctahedral Smectite to Berthierine, Chlorite, Vermiculite, or Saponite. Clays and Clay Minerals, 58, 280-291

Mosser-Ruck, R., Pironon, J., Cathelineau, M., and Trouiller, A. (2001) Experimental illitization of smectite in a K-rich solution. European Journal of Mineralogy, 13, 829-840.

Neuhoff, P.S., Hovis, G.L., Balassone, G., and Stebbins, J.F. (2004) Thermodynamic properties of analcime solid solutions. American Journal of Science, 304, 21-66.

Nutt, M. Voegele, M., Jové-Colón, C.F., Wang, Y., Howard, R., Blink, J., Liu, H.H., Hardin, E., and Jenni, K. (2011) Used fuel disposition campaign disposal research and development road map (Fuel cycle research and development). Sandia National Laboratory.

Ohmoto, H., Hayashi, K-I, and Kajisa, Y. (1994) Experimental study of the solubilities of pyrite in NaCl-bearing aqueous solutions at 250-350°C. Geochimica et Cosmochimica Acta, 58, 2169-2185.

Perry, E.A. and Hower, J. (1970) Burial diagenesis of Gulf Coast politic sediments. Clays and Clay Minerals, 18, 165-177.

Pouchou, J.L. and Pichoir, F. (1985) "PAP" $\phi(\rho z)$ correction procedure for improved quantitative microanalysis. Microbeam Analysis. Ed. Armstrong, J.T. San Francisco Press, pp. 104-106.

Pusch, R (2008) Geological Storage of Radioactive Waste. Springer-Verlag, Berlin, Germany, pp. 379.

Pusch, R. (1979) Highly compacted sodium bentonite for isolating rock-deposited radioactive waste products. Nuclear Technology, 45, 153-157.

Pusch, R. (2001) The microstructure of MX-80 clay with respect to its bulk physical properties under different environmental conditions. Svensk Kärnbränslehantering Technical Report, TR-01-08, pp. 111.

Pusch, R. and Kasbohm, J. (2002) Alteration of MX-80 by hydrothermal treatment under high salt content conditions. Svensk Kärnbränslehantering Technical Report, TR-02-06, pp. 44.

Pusch, R., Takase, H., and Benbow, S. (1998) Chemical processes causing cementation in heat-affected smectite – the Kinnekulle bentonite. Svensk Kärnbränslehantering Technical Report, TR-98-25, pp. 56.

Reynolds, R.C. and Hower, J. (1970) The nature of interlayering in mixed-layer illite-montmorillonite. Clays and Clay Minerals, 18, 25-36.

Rimstidt J.D. and Barnes, H.L. (1980) The kinetics of silica-water reactions. Geochimica et Cosmochimica Acta, 44, 1683-1699.

Roberson, H.E. and Lahann, R.W (1981) Smectite to illite conversion rates: Effects of solution chemistry. Clays and Clay Minerals, 29, 129-135.

Seyfried, J.R., Janecky, D.R., and Berndt, M.E. (1987) Rocking autoclaves for hydrothermal experiments II. The flexible reaction-cell system. Hydrothermal Experimental Techniques. Eds. Ulmer, G.C. and Barnes, H.L. John Wiley & Sons, pp. 216 – 239.

Small, J.S. (1993) Experimental determination of the rates of precipitation of authigenic illite and kaolinite in the presence of aqueous oxalate and comparison to the K/Ar ages of authigenic illite in reservoir sandstones. Clays and Clay Minerals, 41, 191-208.

Small, J.S., Hamilton, D.L., and Habesch, S. (1992) Experimental simulation of clay precipitation within reservoir sandstones 2: Mechanism of illite formation and controls on morphology. Journal of Sedimentary Petrology, 62, 520-529.

Smyth, J.R. (1982) Zeolite stability constraints on radioactive waste isolation in zeolite-bearing volcanic rocks. Journal of Geology, 90, 195-201.

Środoń, J. (1980) Precise identification of illite/smectite interstratifications by X-ray powder diffraction. Clays and Clay Minerals, 28, 401-411.

Środoń, J. (1999) Nature of mixed-layer clays and mechanisms of their formation and alteration. Annual Review of Earth and Planetary Sciences, 27, 19-53.

Villar, M.V., Gómez-Espina, R., and Gutiérrez-Nebot, L. (2012) Basal spacings of smectite in compacted bentonite. Applied Clay Science, 65-66, 95-105.

Wersin, P., Johnson, L.H., and McKinley, I.G. (2007) Performance of the bentonite barrier at temperatures beyond 100°C: A critical review. Physics and Chemistry of the Earth, 32, 780-788.

796 Whitney, G. and Velde, B. (1993) Changes in particle morphology during illitization: An
797 experimental study. Clays and Clay Minerals, 41, 209-218.

798 Wilkin, R.T. and Barnes, H.L. (1998) Solubility and stability of zeolites in aqueous solution: I.
799 Analcime, Na-, and K-clinoptilolite. American Mineralogist, 83, 746-761.

800 Wilkin, R.T. and Barnes, H.L. (2000) Nucleation and growth kinetics of analcime from precursor
801 Na-clinoptilolite. American Mineralogist, 85, 1329-1341.

802 Wilson, J., Savage, D., Cuadros, J., Shibata, M., and Ragnarsdottir, K. (2006a) The effect of iron
803 on montmorillonite stability. (I) Background and thermodynamic considerations.
804 Geochimica et Cosmochimica Acta, 70, 323-336.

805 Wilson, J., Gressey, G., Cressey, B., Cuadros, J., Ragnarsdottir, K., Savage, D., and Shibata, M.
806 (2006b) The effect of iron on montmorillonite stability. (II) Experimental investigation.
807 Geochimica et Cosmochimica Acta, 70, 306-322.

808 Wolery, T.W. and Jarek, R.L. (2003) EQ3/6, Version 8.0, SOFTWARE USER'S MANUAL,
809 Prepared for U.S. Department of Energy, Office of Civilian Radioactive Waste
810 Management by Sandia National Laboratories, Albuquerque, New Mexico, pp. 376.

811 Zhang G., Kim, J., Dong, H., and Sommer, A. (2007) Microbial effects in promoting the smectite
812 to illite reaction: Role of organic matter intercalated in the interlayer. American
813 Mineralogist, 92, 1401-1410.

814

List of figures captions

Figure 1. Heating profile used for ramped and isothermal experiments.

Figure 2. Minerals associated with unreacted Colony, WY bentonite A) typical montmorillonite foily morphology with plagioclase and possibly cristobalite/opal-C, B) tabular clinoptilolite replacing precursor volcanic shards, C) framboidal pyrite, and D) cubic pyrite.

Figure 3. XRD patterns of glycolated (oriented) pre- and post-reaction montmorillonite (GS) from the ramped thermal profile experiments shows no montmorillonite alteration to illite or illite/smectite. d-spacings and n^{th} 00ℓ order have been labeled above each peak. Minor amounts of clinoptilolite (*), cristobalite/opal-C (**), and quartz (***) are also present in the < 2 μm fraction.

Figure 4. Post-reaction mineralogical characteristics from ramp heating experiments A) typical montmorillonite foily morphology from EBS-2, B) montmorillonite foily morphology with biotite and feldspars from EBS-2, and C) authigenic albitic plagioclase embedded in montmorillonite from EBS-1.

Figure 5. XRD patterns of glycolated (oriented) pre- and post-reaction montmorillonite (GS) from the isothermal, 300°C thermal profile experiments shows no montmorillonite alteration to illite or illite/smectite. d-spacings and n^{th} 00ℓ order have been labeled above each peak. A small, 10 Å peak (possibly illite) appears to be present in EBS-5 material. Minor amounts of clinoptilolite (*), cristobalite/opal-C (**), quartz (***), and halite (#) are also present in the < 2 μm fraction.

Figure 6. Post-reaction SEM images showing mineralogical characteristics from the isothermal 300°C experiments including A) montmorillonite foils displaying partially deteriorated edges, B) bundle of authigenic fibrous illite, C) authigenic albitic plagioclase overgrowths showing possible polysynthetic twinning, D) subhedral analcime formed from the dissolution of clinoptilolite, and E) backscatter electron image showing discrete analcime crystals, various stages of clinoptilolite dissolution, and clinoptilolite replacement by analcime.

Figure 7. A) Na^+ and K^+ and B) $SiO_{2(aq)}$ raw concentrations through the ramped experiments (EBS-3 and EBS-4) showing evolution of solutes in contact with bentonite. Quenching experiment to room temperature significantly changes the solution chemistry (Q). Error bars represent analytical uncertainty of 1 σ.

Figure 8. A) Na^+ and K^+ and B) $SiO_{2(aq)}$ raw concentrations through the isothermal 300°C long-term experiments (EBS-5, EBS-10, and EBS-11) showing evolution of solutes in contact with bentonite. Quenching experiment to room temperature significantly changes the solution chemistry (Q). Error bars represent analytical uncertainty of 1 σ.

Figure 9. Evolution of (A) Sulfate and (B) aluminum (right) solution concentration during the ramped and isothermal experiments. Quenching experiment to room temperature significantly changes the solution chemistry (Q). Error bars represent analytical uncertainty of 1 σ.

Figure 10. Log aNa^+/aH^+ and log $aSiO_{2(aq)}$ data from 120°C solution chemistries, 210°C solution chemistries, and 300°C solution chemistries compared to Na-H_2O-SiO_2 phase relations at vapor-saturated pressures. Analcime thermodynamic data has been adjusted to a high-silicon analcime ($Na_{0.75}Al_{0.75}Si_{2.25}O_6 \cdot 1.13H_2O$) after Neuhoff et al. (2004). Quartz (qtz), cristobalite (crist), and amorphous silica (am SiO2) data are from Rimstidt and Barnes (1980). Natrolite was suppressed.

Figure 11. Log aK^+/aH^+ and log $aSiO_{2(aq)}$ data from 120°C solution chemistries, 210°C solution chemistries, and 300°C solution chemistries compared to K-H_2O-SiO_2 phase relations at vapor-saturated pressures. Illite ($K_{0.85}Al_2(Si_{3.15}Al_{0.85})O_{10}(OH)_2$) thermodynamic data is from Blanc and Vieillard (2010). Quartz (qtz), cristobalite (crist), and amorphous silica (am SiO2) data are from Rimstidt and Barnes (1980). Muscovite was suppressed to show the illite stability field.

Appendix

EMP standards and oxide detection limits for silicate analyses

Phlogopite (Synthetic): MgO = 0.02 wt.% , F = 0.11 wt.%

Albite (Amelia, NC, U.S.A, Rutherford mine): Na_2O = 0.02 wt.%

Labrodorite (Chihuahua, Mexico): Al_2O_3 = 0.02 wt.%, SiO_2 = 0.02 wt.%, CaO = 0.01 wt.%

Tugtupite (Greenland): Cl = 0.01 wt.%

Adularia (St. Gotthard, Switzerland): K_2O = 0.01 wt.%

Titanite glass (Penn State): TiO_2 = 0.02 wt.%

MagnesioChromite (Synthetic): Cr_2O_3 = 0.04 wt.%

Rhodonite (unknown locality): MnO = 0.02 wt.%

Augite (unknown locality): FeO = 0.02 wt.%

Liebenbergite (synthetic): NiO = 0.06 wt.%

Gahnite: ZnO = 0.05 wt.%

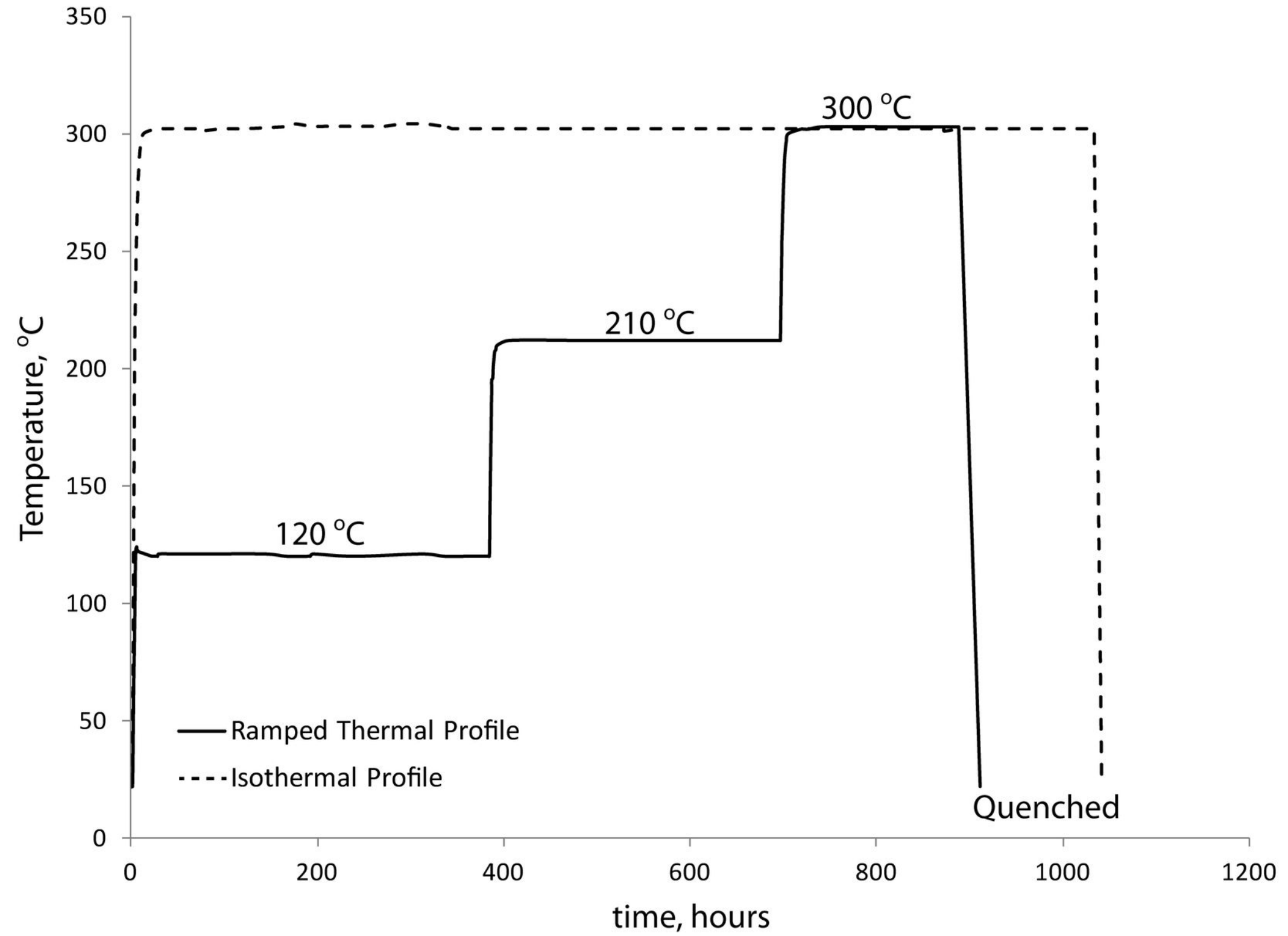
350
300
250
200
150
100
50
0
Temperature, °C
300 °C
210 °C
120 °C
Ramped Thermal Profile
Isothermal Profile
Quenched
0
200
400
600
800
1000
1200
time, hours

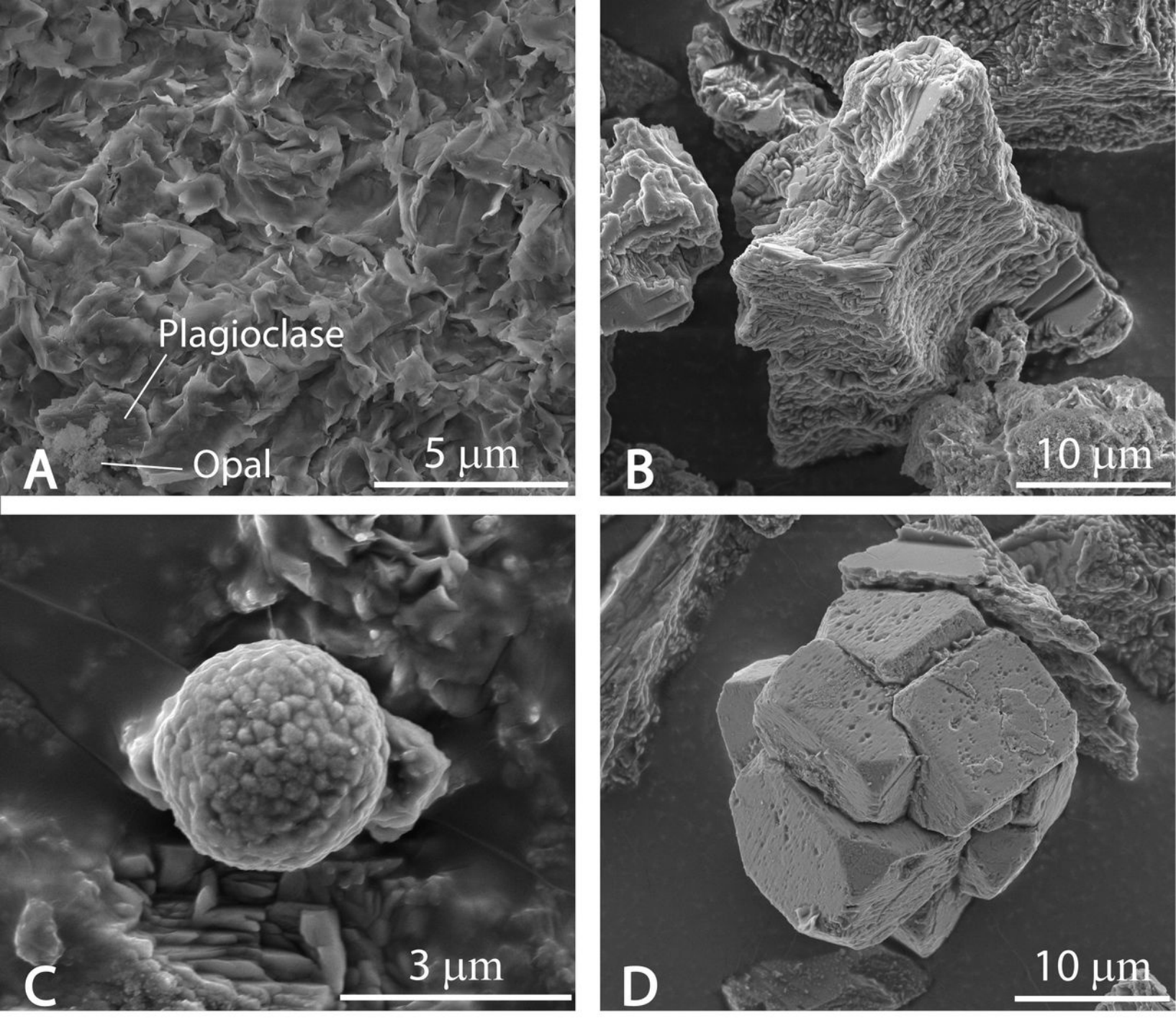
Plagioclase
Opal
A
5 µm
B
10 µm
C
3 µm
D
10 µm

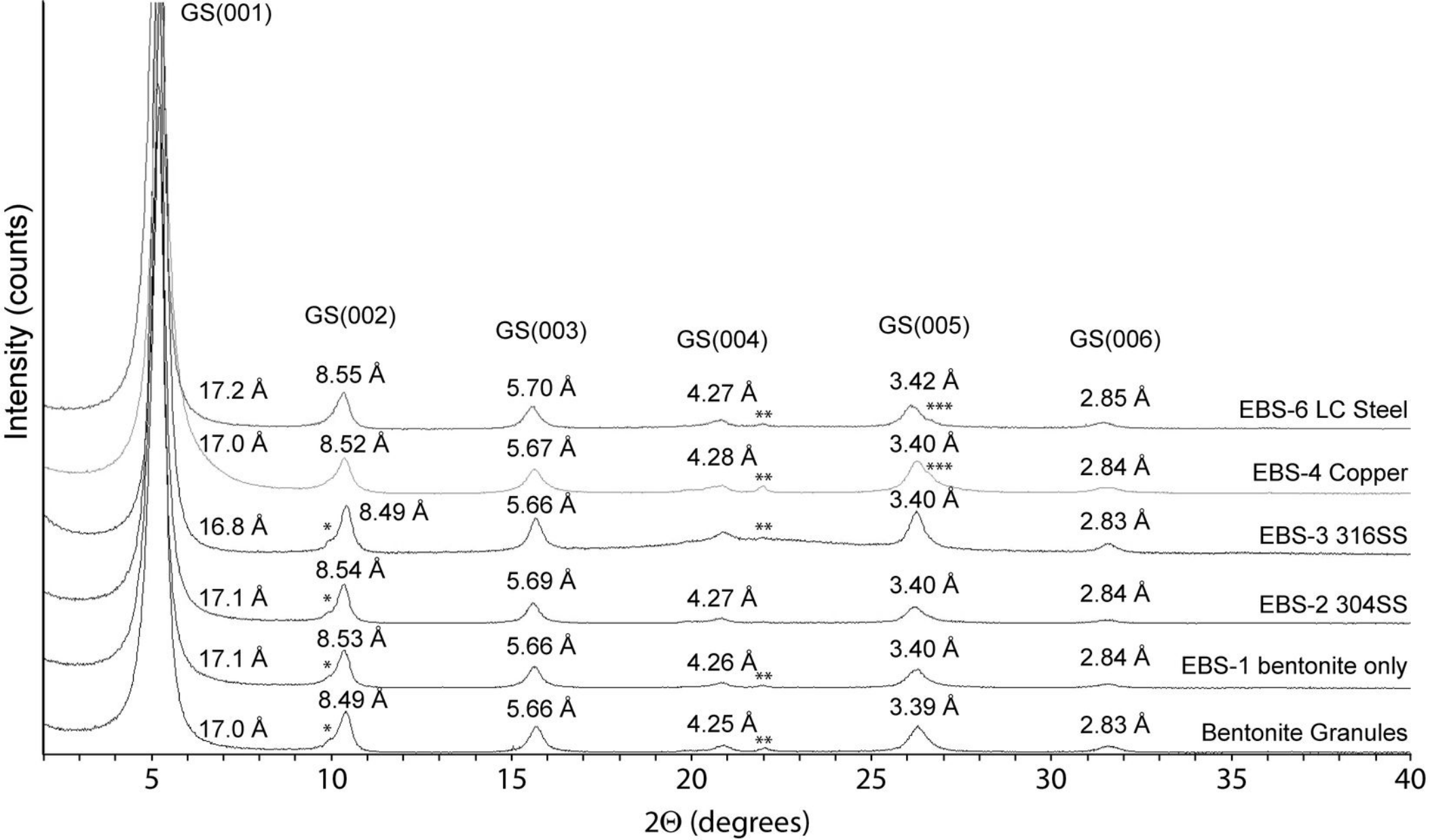
GS(001)
GS(002)
GS(003)
GS(004)
GS(005)
GS(006)
17.2 Å
8.55 Å
5.70 Å
4.27 Å
3.42 Å
2.85 Å
EBS-6 LC Steel
17.0 Å
8.52 Å
5.67 Å
4.28 Å
3.40 Å
2.84 Å
EBS-4 Copper
16.8 Å
8.49 Å
5.66 Å
3.40 Å
2.83 Å
EBS-3 316SS
17.1 Å
8.54 Å
5.69 Å
4.27 Å
3.40 Å
2.84 Å
EBS-2 304SS
17.1 Å
8.53 Å
5.66 Å
4.26 Å
3.40 Å
2.84 Å
EBS-1 bentonite only
17.0 Å
8.49 Å
5.66 Å
4.25 Å
3.39 Å
2.83 Å
Bentonite Granules
Intensity (counts)
2Θ (degrees)
5
10
15
20
25
30
35
40

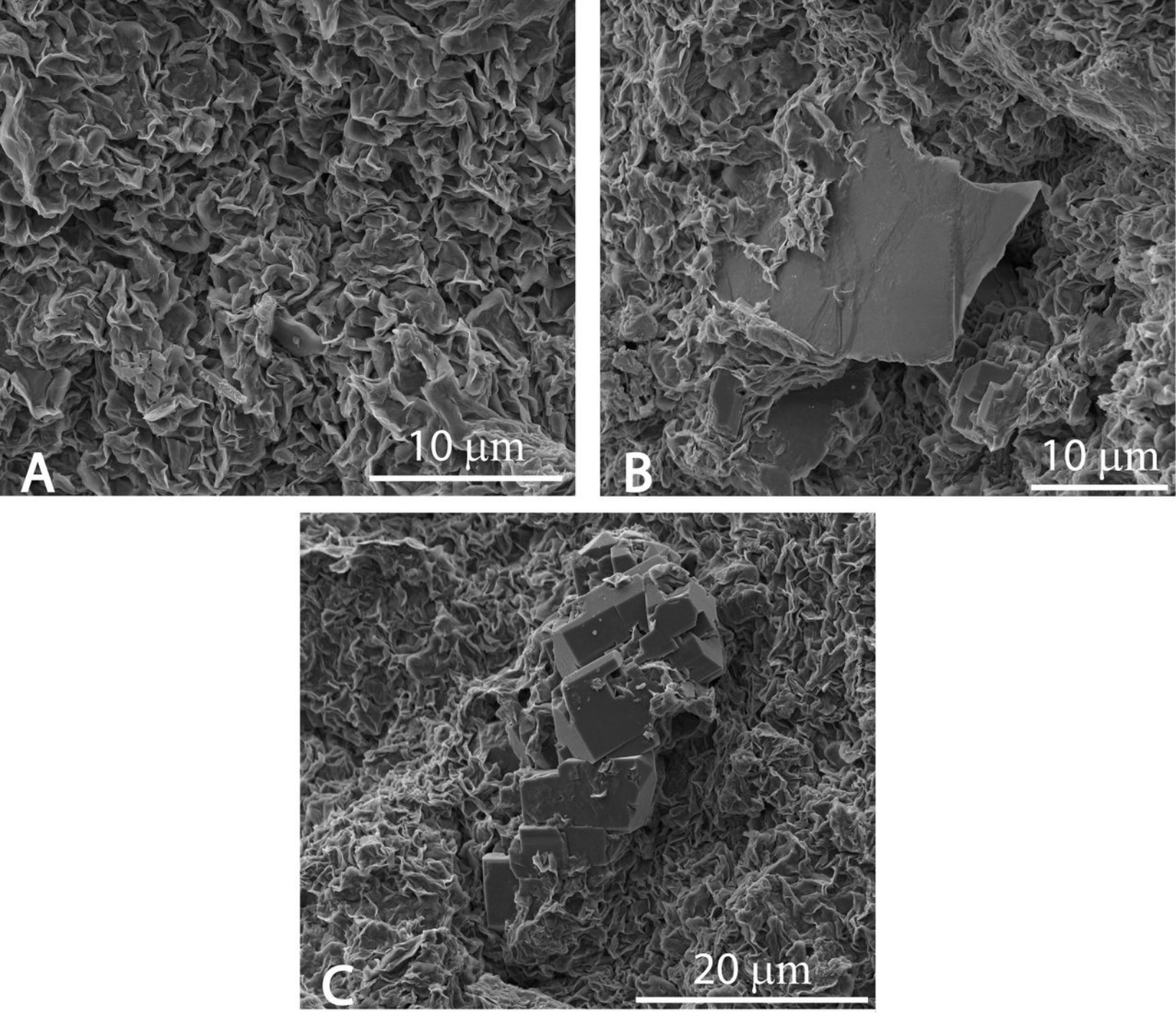
A
10 µm
B
10 µm
C
20 µm

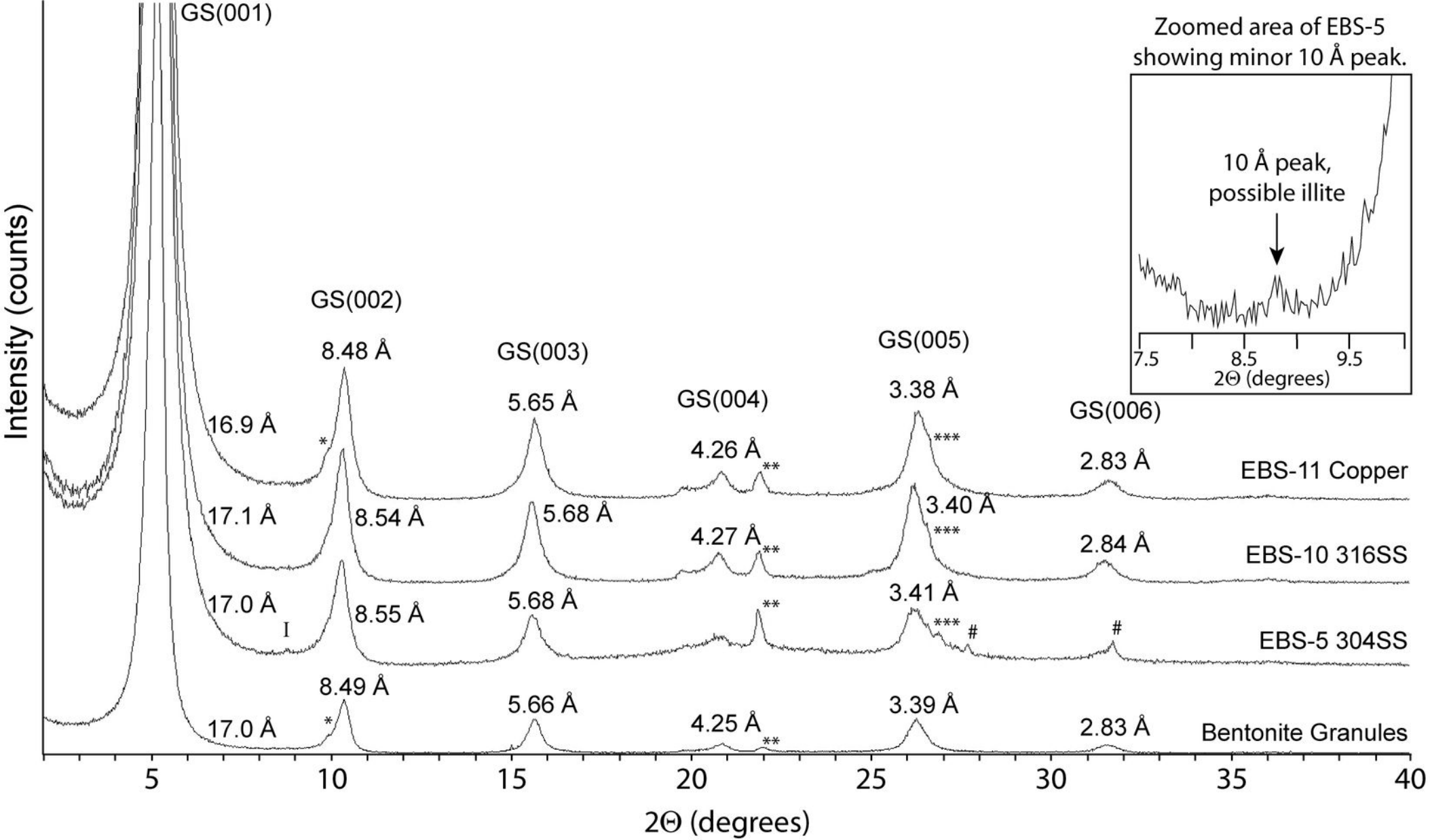
GS(001)
GS(002)
8.48 Å
GS(003)
5.65 Å
GS(004)
4.26 Å
GS(005)
3.38 Å
GS(006)
2.83 Å
16.9 Å
EBS-11 Copper
17.1 Å
8.54 Å
5.68 Å
4.27 Å
3.40 Å
2.84 Å
EBS-10 316SS
17.0 Å
I
8.55 Å
5.68 Å
3.41 Å
EBS-5 304SS
8.49 Å
17.0 Å
5.66 Å
4.25 Å
3.39 Å
2.83 Å
Bentonite Granules
Zoomed area of EBS-5
showing minor 10 Å peak.
10 Å peak,
possible illite
7.5
8.5
9.5
2Θ (degrees)
Intensity (counts)
5
10
15
20
25
30
35
40
2Θ (degrees)

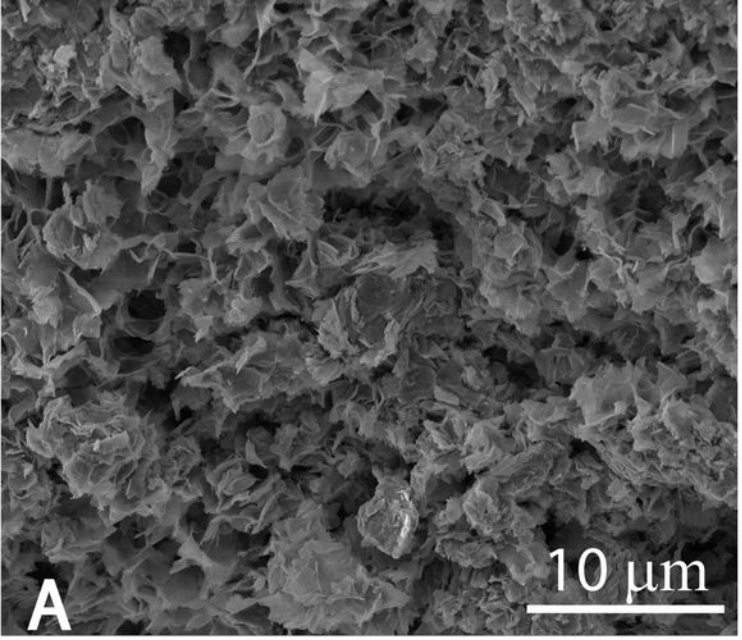
10 μm
A

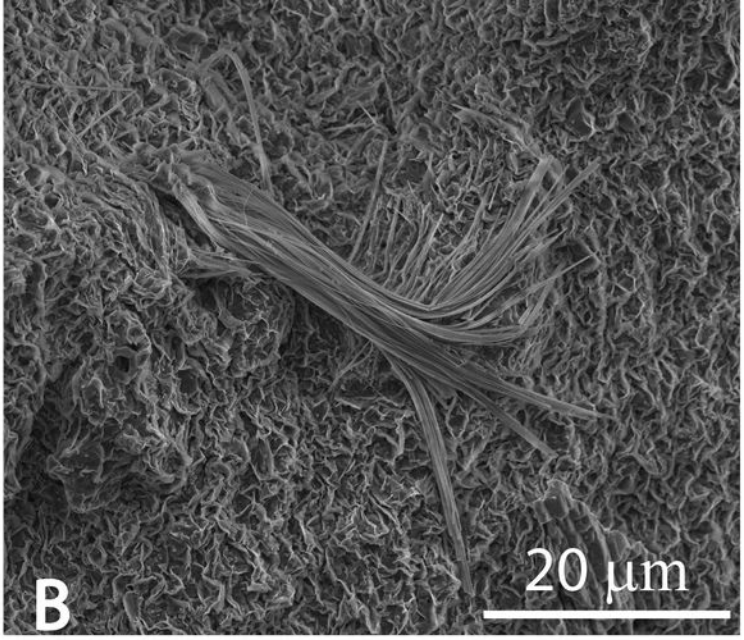
20 μm
B

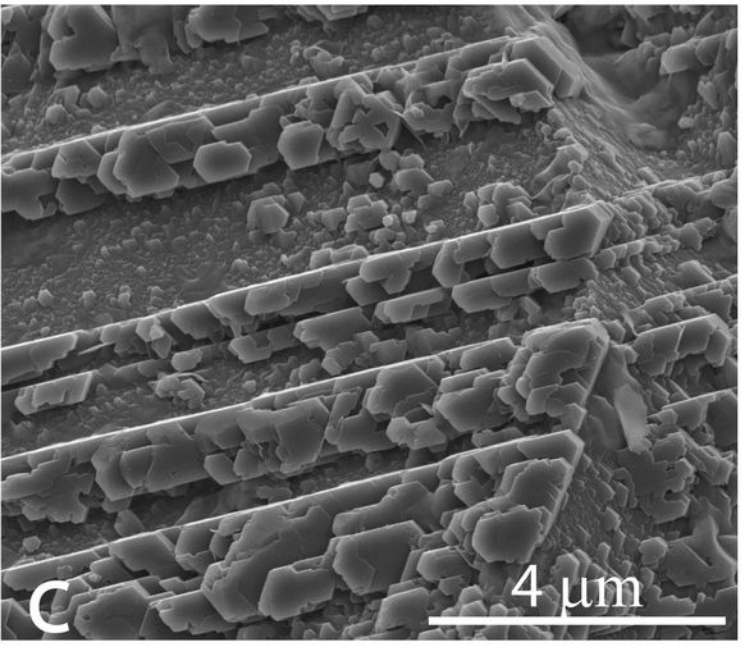
4 μm
C

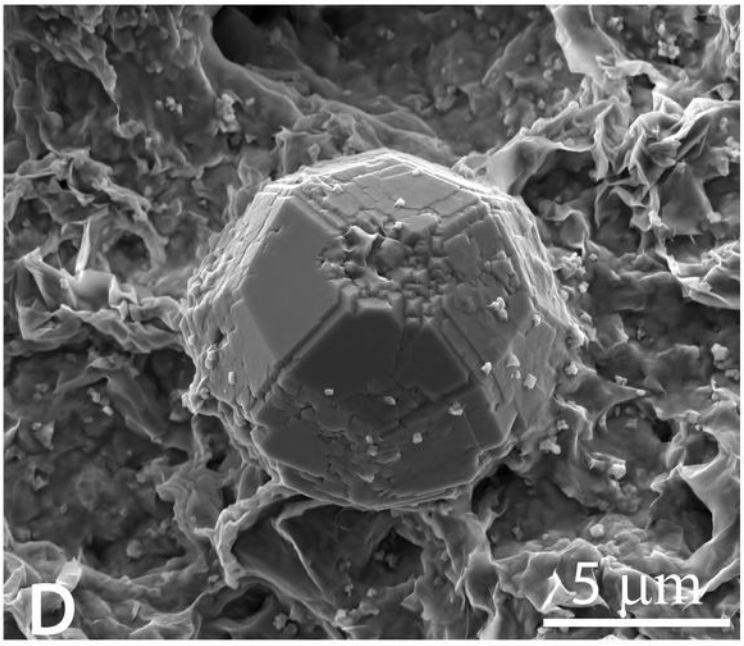
5 μm
D

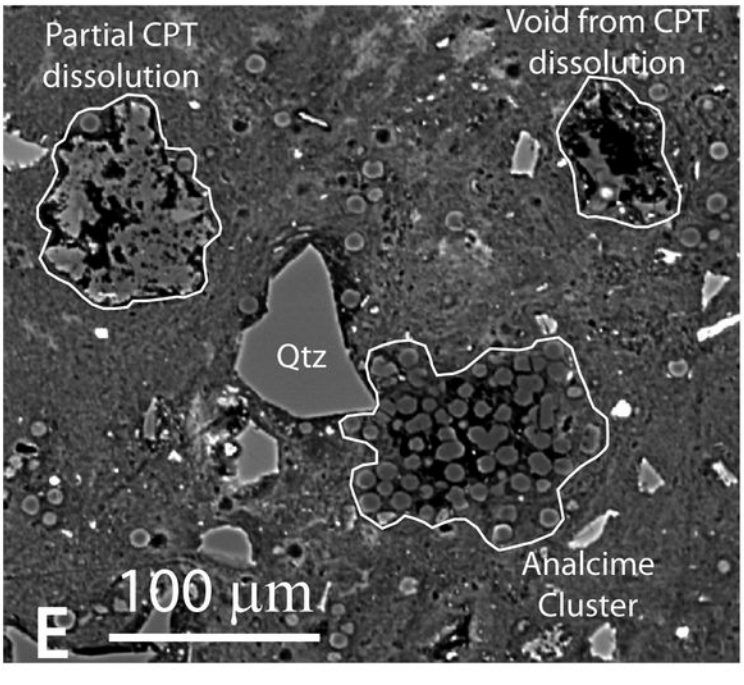
Partial CPT dissolution
Void from CPT dissolution
Qtz
Analcime Cluster
100 μm
E

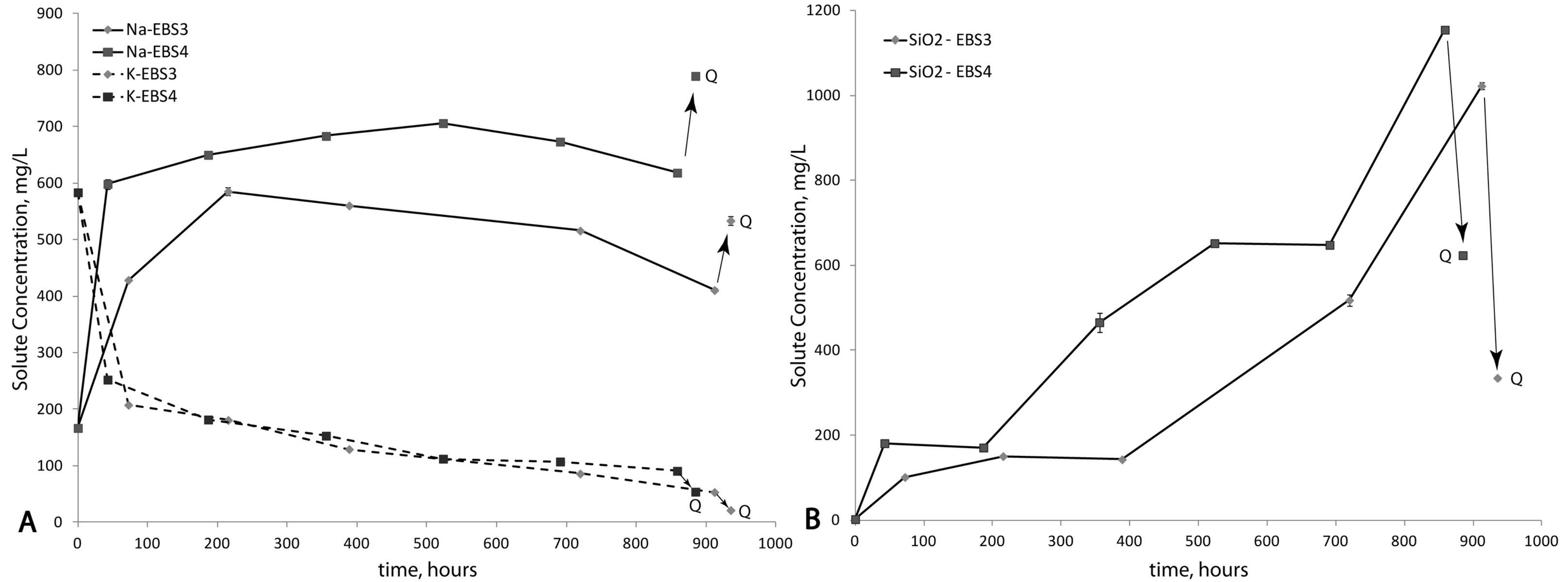
Na-EBS3
Na-EBS4
K-EBS3
K-EBS4
Solute Concentration, mg/L
time, hours
Q
A
SiO2 - EBS3
SiO2 - EBS4
Solute Concentration, mg/L
time, hours
Q
B

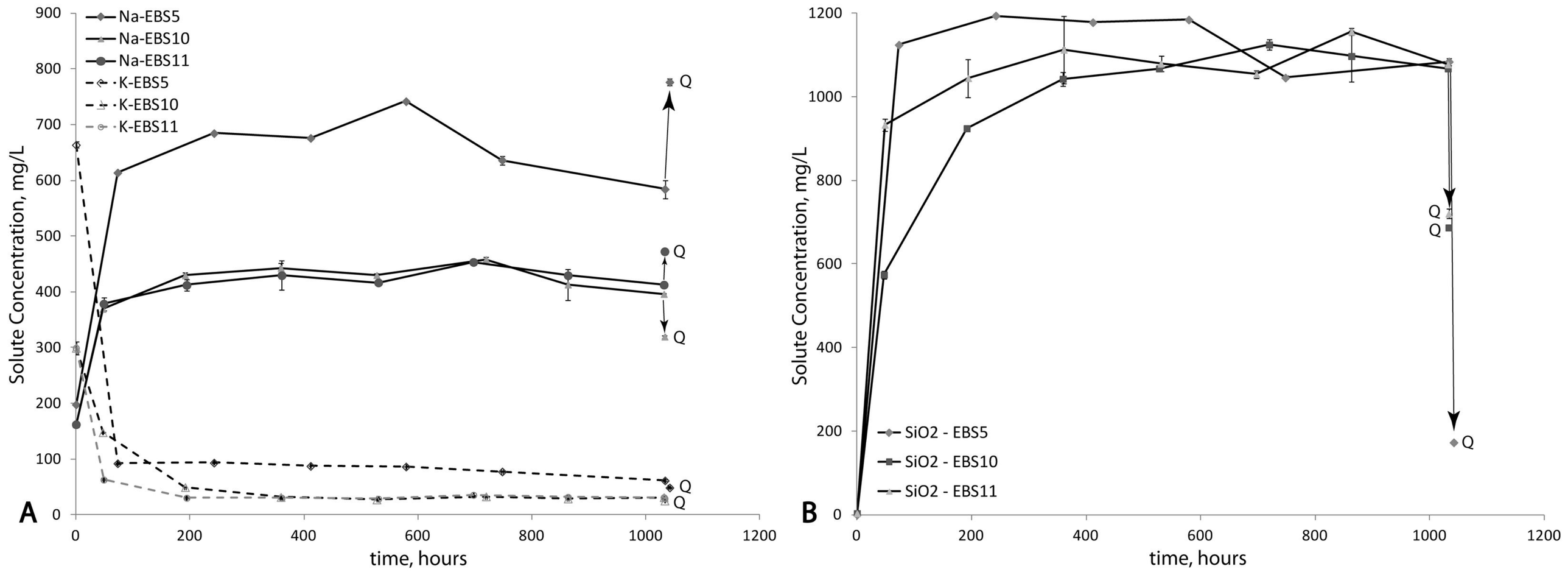
Na-EBS5
Na-EBS10
Na-EBS11
K-EBS5
K-EBS10
K-EBS11
Solute Concentration, mg/L
time, hours
A
Q
SiO2 - EBS5
SiO2 - EBS10
SiO2 - EBS11
B

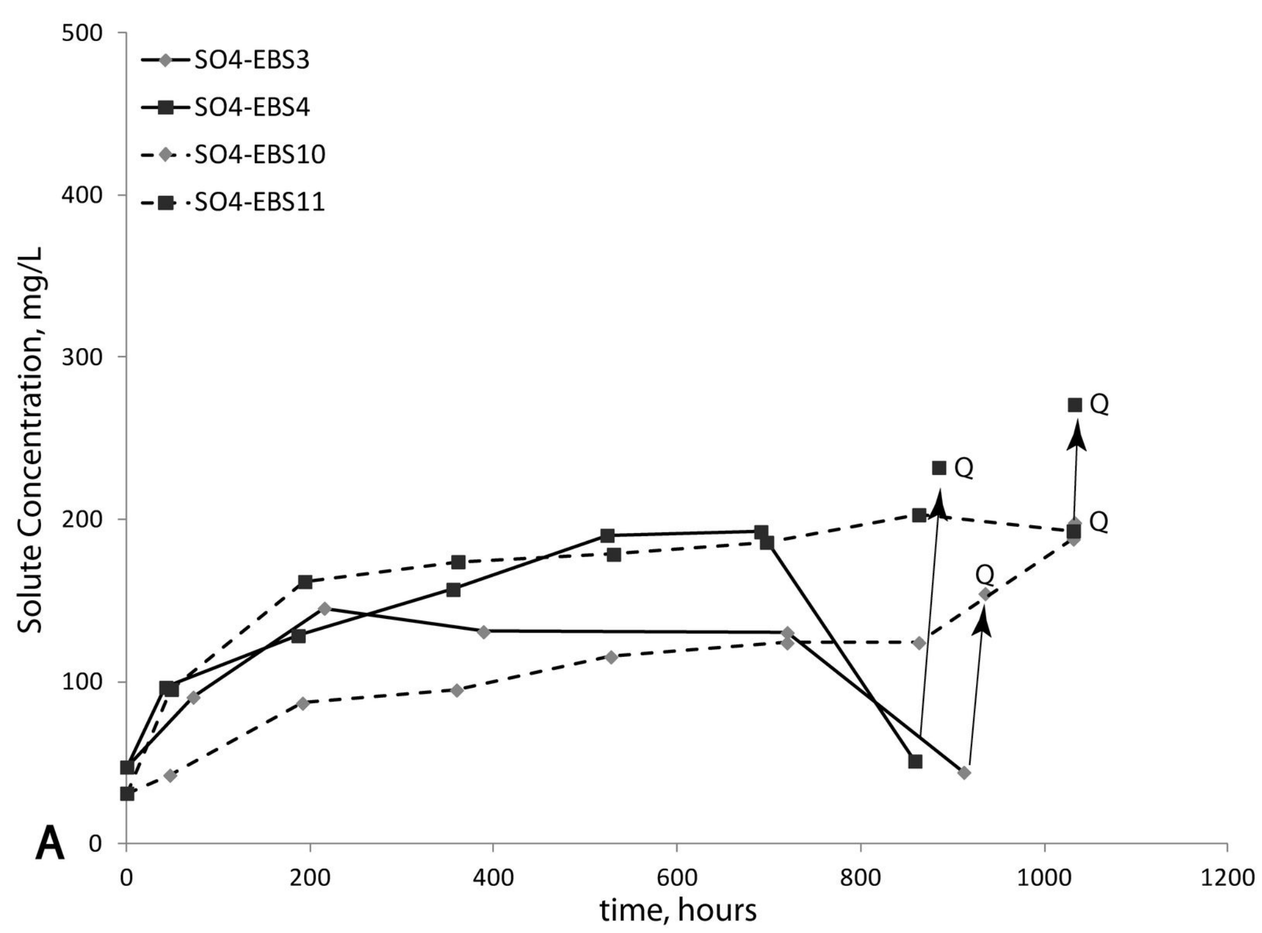
SO4-EBS3
SO4-EBS4
SO4-EBS10
SO4-EBS11
Solute Concentration, mg/L
time, hours
A
Q
Q
Q
Q

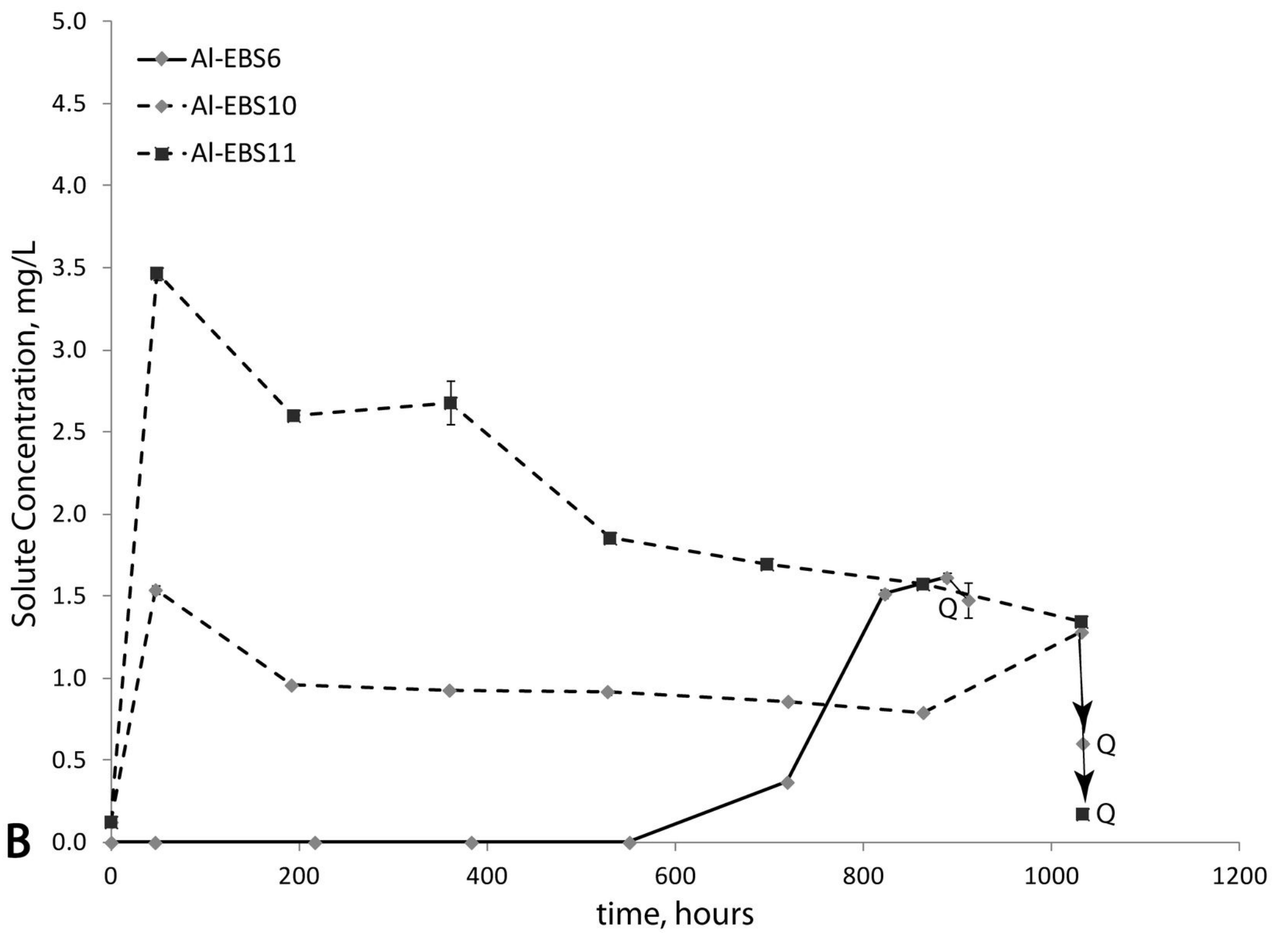
Al-EBS6
Al-EBS10
Al-EBS11
Solute Concentration, mg/L
time, hours
B
Q
Q
Q

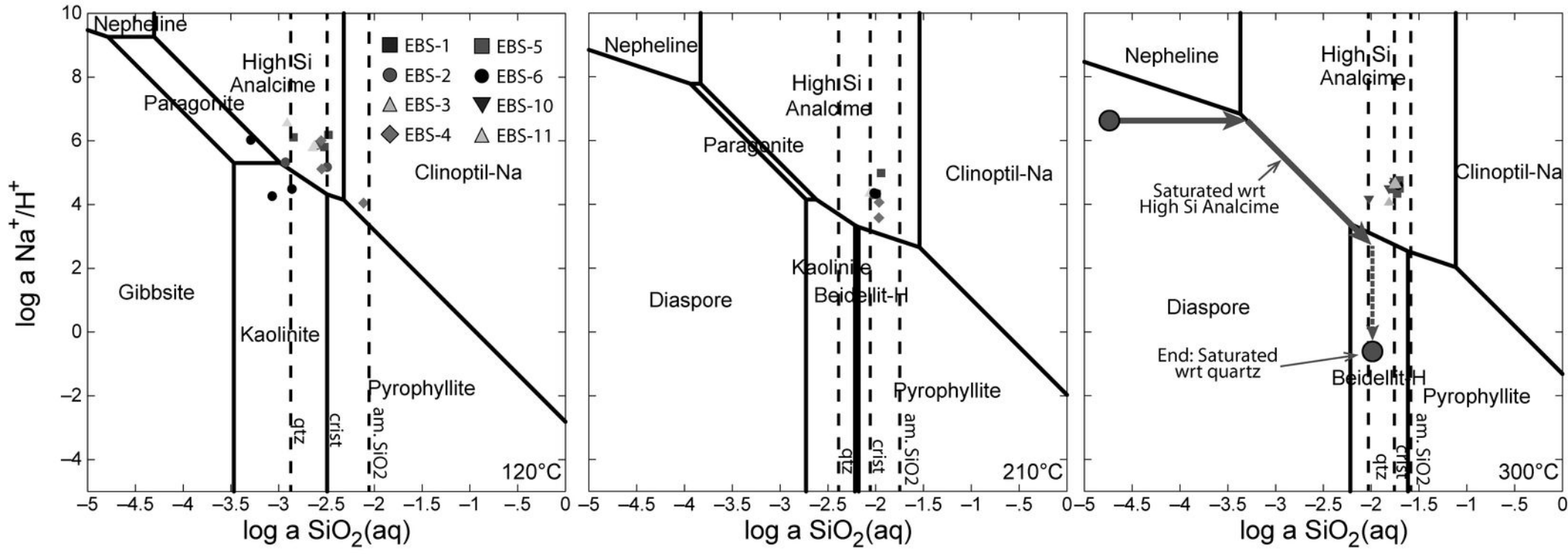
Nepheline
High Si Analcime
Paragonite
Clinoptil-Na
Gibbsite
Kaolinite
Pyrophyllite
Diaspore
Beidellit-H
EBS-1
EBS-2
EBS-3
EBS-4
EBS-5
EBS-6
EBS-10
EBS-11
qtz
crist
am. SiO2
120°C
210°C
300°C
Saturated wrt High Si Analcime
End: Saturated wrt quartz
log a Na+/H+
log a SiO2(aq)

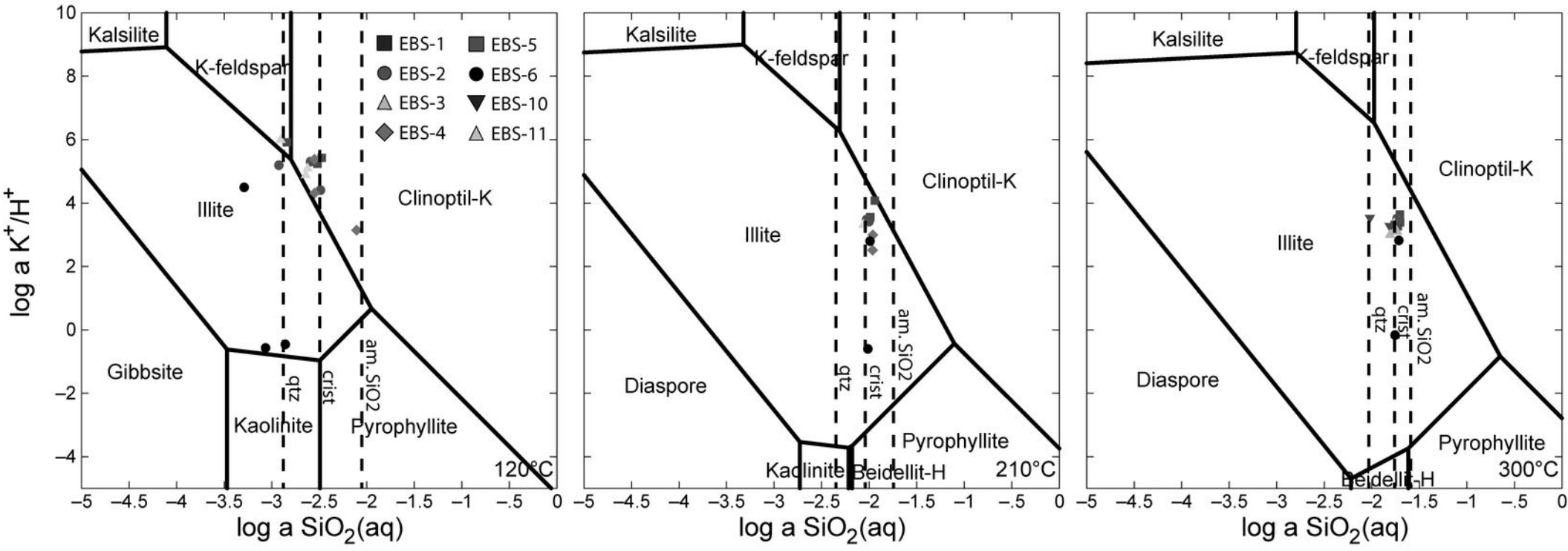
Kalsilite
K-feldspar
Illite
Clinoptil-K
Gibbsite
Kaolinite
Pyrophyllite
Diaspore
Kaolinite
Beidellit-H
qtz
crist
am. SiO2
bzi
EBS-1
EBS-2
EBS-3
EBS-4
EBS-5
EBS-6
EBS-10
EBS-11
120°C
210°C
300°C
log a K+/H+
log a SiO2(aq)

Tables

Table 1. Synthetic groundwater chemistries used in the hydrothermal experiments. All values were measured at 25°C.

	Stripa V2.1	Stripa V2.2
Species	mg/L	mg/L
Ca^{2+}	89	43
Cl^{-}	1045	686
K^{+}	583	299
Na^{+}	167	162
Si	1	2
SO_4^{2-}	47	31
Sr^{2+}	0.05	<0.05
TDS	1934	1226
pH	8.59	8.40
Experiment Used	EBS 1-5	EBS 6, 10-11

Table 2. Reactants and reaction conditions for EBS experiments.

	Bentonite, g	Brine, g	Brine Type	Fe°, g	Fe_3O_4, g	Component, g	EBS Component	Run temp, °C	Run time
EBS-1	7.4	79.0	Stripa V2.1	0.257	0.252	na	na	25/100/200/300/25	4 weeks
EBS-2	7.2	62.0	Stripa V2.1	0.251	0.253	4.980	304SS	25/100/200/300/25	4 weeks
EBS-3	6.790	59.4	Stripa V2.1	0.255	0.261	4.245	316SS	25/100/200/300/25	5 weeks
EBS-4	16.207	145.0	Stripa V2.1	0.574	0.579	9.753	Copper	25/100/200/300/25	5 weeks
EBS-6	12.109	104.2	Stripa V2.2	0.424	0.424	8.375	Low-C Steel	25/100/200/300/25	5 weeks
EBS-5	15.770	135.9	Stripa V2.1	0.505	0.505	11.189	304SS	300	6 weeks
EBS-10	21.105	182.3	Stripa V2.2	0.675	0.675	14.937	316SS	300	6 weeks
EBS-11	15.039	129.8	Stripa V2.2	0.481	0.481	10.643	Copper	300	6 weeks

Table 3. Bulk mineralogical composition (wt. %) of the starting bentonite and post-reaction samples. b.d.l. indicates below detection limits. "+" indicates present but is < 0.5 wt. %. The average mineral abundance error for each phase is approximately ±1 wt. % non-clay minerals and ±5 wt. % for clay minerals.

	Initial	Ramped heating 120 to 300°C					Isothermal 300°C		
	Bentonite	EBS-1	EBS-2	EBS-3	EBS-4	EBS-6	EBS-5	EBS-10	EBS-11
Metal Plates	--	--	304SS	316SS	Cu	LC Steel	304SS	316SS	Cu
Montmorillonite	72	81	75	79	79	81	79	79	80
Quartz	1	2	1	2	1	2	2	3	2
Cristobalite/Opal-C	2	2	3	2	1	4	4	2	2
Clinoptilolite	13	8	9	6	6	7	2	6	8
Analcime	**b.d.l.**	**b.d.l.**	**b.d.l.**	**b.d.l.**	**b.d.l.**	**b.d.l.**	3	1	1
Feldspar	9	6	9	8	9	4	7	8	7
Biotite	3	2	4	1	2	1	2	1	+
Illite	**b.d.l.**	**b.d.l.**	**b.d.l.**	**b.d.l.**	**b.d.l.**	**b.d.l.**	+	**b.d.l.**	**b.d.l.**
Pyrite	0.4	**b.d.l.**	**b.d.l.**	**b.d.l.**	**b.d.l.**	**b.d.l.**	**b.d.l.**	**b.d.l.**	**b.d.l.**
Magnetite	**b.d.l.**	**b.d.l.**	**b.d.l.**	2	1	+	1	**b.d.l.**	**b.d.l.**
Halite	**b.d.l.**	**b.d.l.**	**b.d.l.**	**b.d.l.**	+	**b.d.l.**	+	**b.d.l.**	**b.d.l.**

Table 4. XRD result of the initial bentonite and post-reaction samples showing °2Θ positions and Δ°2Θ (002/003) values for the (00ℓ) reflections from the oriented, ethylene glycol saturated, < 2 μm fraction. Expandable component (%) calculated from regression equations determined via [1]Eberl et al. 1993 and [2]Moore and Reynolds 1997.

	°2Θ				Δ°2Θ	% Exp		
	001	**002**	**003**	**005**	**002/003**	**1, Eq. 3**	**1, Eq. 4**	**2**
Initial Bentonite	5.20	10.42	15.66	26.27	5.24	101	103	104
EBS-1	5.17	10.37	15.66	26.20	5.29	98	100	101
EBS-2	5.16	10.35	15.58	26.18	5.23	102	104	105
EBS-3	5.26	10.42	15.65	26.23	5.23	101	104	104
EBS-4	5.19	10.38	15.62	26.22	5.24	101	103	104
EBS-6	5.15	10.34	15.55	26.08	5.21	103	105	106
EBS-5	5.19	10.34	15.61	26.13	5.27	99	101	102
EBS-10	5.18	10.36	15.60	26.18	5.24	101	103	104
EBS-11	5.22	10.43	15.69	26.33	5.26	100	102	103

Table 5. Chemical composition (XRF) of the starting bentonite and < 2 μm size fractions from post-reaction samples from each EBS experiment. Bulk bentonite composition is an average of four samples (n = 4) collected after cone and quartering of the stock bentonite. Oxides and loss on ignition (LOI) are presented as wt. % wt.% and trace element data are presented as ppm. *Total iron is represented as Fe_2O_3. b.d.l. indicates below detection limits.

	Initial Bentonite		Ramped heating 120 to 300 °C					Isothermal 300 °C				
	bulk	< 2 μm	EBS-1 < 2 μm	EBS-2 < 2 μm	EBS-3 < 2 μm	EBS-4 < 2 μm	EBS-6 < 2 μm	EBS-5 < 2 μm	EBS-10 < 2 μm	EBS-11 < 2 μm	Detection	
Metal	n = 4		none	304SS	316SS	Cu	LC Steel	304SS	316SS	Cu	Limits	
fuse ratio	7:1	36:1	36:1	36:1	36:1	36:1	36:1	36:1	36:1	36:1	36:1	Error, ±
Na_2O	2.85	2.57	2.35	2.10	2.22	2.40	2.23	2.39	2.16	2.60	0.16	0.14
MgO	1.64	1.96	2.04	2.00	1.91	1.87	1.84	1.92	1.75	1.81	0.08	0.12
Al_2O_3	19.5	20.9	20.6	20.5	20.6	20.1	19.8	20.9	19.7	19.5	0.07	0.69
SiO_2	61.9	63.3	62.3	63.2	62.5	62.2	63.6	62.8	59.9	63.0	0.29	0.57
P_2O_5	0.044	**b.d.l.**	**b.d.l**	**b.d.l**	**b.d.l.**	**b.d.l.**	**b.d.l.**	**b.d.l.**	**b.d.l.**	**b.d.l.**	0.017	0.006
K_2O	0.572	0.174	0.700	0.660	0.684	0.702	0.982	0.193	0.399	0.345	0.022	0.027
CaO	0.860	0.636	0.736	0.547	0.710	0.746	0.792	0.764	0.721	0.663	0.030	0.039
TiO_2	0.142	0.137	0.121	0.121	0.124	0.132	0.132	0.120	0.122	0.127	0.034	0.004
MnO	0.013	**b.d.l.**	**b.d.l.**	0.015	0.021	0.024	0.018	0.021	0.020	0.017	0.013	0.002
*Fe_2O_3	4.12	4.49	4.55	4.55	5.24	5.87	4.83	5.12	5.45	4.82	0.074	0.08
V	7	**b.d.l.**	**b.d.l.**	**b.d.l.**	**b.d.l.**	**b.d.l.**	**b.d.l.**	**b.d.l.**	**b.d.l.**	**b.d.l.**	44	0
Cr	6	**b.d.l.**	**b.d.l.**	**b.d.l.**	**b.d.l.**	**b.d.l.**	**b.d.l.**	**b.d.l.**	**b.d.l.**	**b.d.l.**	73	1
Ni	5	41	46	56	48	33	47	35	35	41	26	4
Cu	7	54	61	252	94	119	45	55	66	193	27	4
Zn	96	**b.d.l.**	**b.d.l.**	**b.d.l.**	**b.d.l.**	58	**b.d.l.**	**b.d.l.**	34	75	26	12
Rb	18	**b.d.l.**	**b.d.l.**	**b.d.l.**	**b.d.l.**	**b.d.l.**	**b.d.l.**	**b.d.l.**	171	**b.d.l.**	23	5
Sr	297	133	139	164	126	125	215	110	164	134	27	5
Zr	196	144	137	143	150	144	139	149	61	144	30	19
Ba	664	177	149	**b.d.l.**	**b.d.l.**	**b.d.l.**	230	**b.d.l.**	**b.d.l.**	**b.d.l.**	105	34
LOI	8.21	5.76	6.46	6.13	5.85	5.88	5.61	5.69	9.71	6.95		1.71
total	99.990	99.982	99.910	99.884	99.900	99.972	99.901	99.953	99.985	99.891		

Table 6. Structural formula for initial and post-reaction montmorillonites. Structural formulas were calculated following the method described by Moore and Reynolds (1997).

Run Conditions	Run #	Metal Plate	Montmorillonite Structural Formulae
Initial Bentonite	Na	Na	$(Na_{0.31},Ca_{0.04},K_{0.01})(Al_{1.53},Fe_{0.21},Mg_{0.18},Ti_{.01})(Si_{3.98},Al_{0.02})O_{10}(OH)_2$
Ramped, 120 to 300°C 150 – 160 bar 5 weeks	EBS-1	none	$(Na_{0.29},K_{0.06},Ca_{0.05})(Al_{1.51},Fe^{3+}_{0.22},Mg_{0.19},Ti_{0.01})(Si_{3.96},Al_{0.04})O_{10}(OH)_2$
	EBS-2	304SS	$(Na_{0.26},K_{0.04},Ca_{0.05})(Al_{1.53},Fe^{3+}_{0.22},Mg_{0.19},Ti_{0.01})(Si_{4.00})O_{10}(OH)_2$
	EBS-3	316SS	$(Na_{0.27},K_{0.06},Ca_{0.05})(Al_{1.50},Fe^{3+}_{0.25},Mg_{0.18},Ti_{0.01})(Si_{3.96},Al_{0.04})O_{10}(OH)_2$
	EBS-4	copper	$(Na_{0.30},K_{0.06},Ca_{0.05})(Al_{1.46},Fe^{3+}_{0.28},Mg_{0.18},Ti_{0.01})(Si_{3.95},Al_{0.05})O_{10}(OH)_2$
	EBS-6	low-C Steel	$(Na_{0.27},K_{0.08},Ca_{0.05})(Al_{1.47},Fe^{3+}_{0.23},Mg_{0.17},Ti_{0.01})(Si_{4.02})O_{10}(OH)_2$
Isothermal, 300°C 150 – 160 bar 6 weeks	EBS-5	304SS	$(Na_{0.31},K_{0.02},Ca_{0.05})(Al_{1.46},Fe^{3+}_{0.26},Mg_{0.19},Ti_{0.01})(Si_{3.83},Al_{0.17})O_{10}(OH)_2$
	EBS-10	316SS	$(Na_{0.28},K_{0.03},Ca_{0.05})(Al_{1.18},Fe^{3+}_{0.27},Mg_{0.17},Ti_{0.01})(Si_{3.64},Al_{0.36})O_{10}(OH)_2$
	EBS-11	copper	$(Na_{0.33},K_{0.03},Ca_{0.05})(Al_{1.37},Fe^{3+}_{0.24},Mg_{0.18},Ti_{0.01})(Si_{3.85},Al_{0.15})O_{10}(OH)_2$